Investigation of OFDM modulation for radar application

Robin Bengtsson
Emil Bergman

Department of Electrical and Information Technology
Lund University

Supervisor: Fredrik Tufvesson

Examiner: Ove Edfors

June 19, 2024

Printed in Sweden
Tryckeriet i E-huset, Lund

Abstract

The merging of communication and sensing in the same transmission chain has become an increasingly relevant prospect as it allows for better coordination between users at the same time as it more effectively utilize the available frequency bands which are becoming increasingly crowded. Orthogonal frequency division multiplexing (OFDM) radars is one way to combine the two by applying the common modulation scheme to a radar, thus opening up the possibility to extract radar data from a communication transmission. This thesis will present the design, implementation and proof of concept verification of an OFDM radar platform constructed from commercially available antennas, low cost software defined radios (SDRs) and open-source software. The presented platform uses two Yagi-Uda antennas, each connected to an SDR, one for transmission and one for reception, operated by separate host computers. Previous work has investigated, often by use of simulations, the difference in performance between a typical frequency modulated continuous wave (FMCW) radar and an OFDM based radar. Since similar performance is achievable this thesis aims to contribute by comparing the performance effect of sending a chirp-like Zadoff-Chu signal and a communication-like signal with random data over the OFDM channel in terms of people and vehicle detection. The comparison is carried out experimentally in different outdoor environments where each test is recorded both by sending a chirp-like signal and a communication-like signal. The results suggests that there is no apparent difference between the two in regards to detecting persons or vehicles at short range, using the given setup.

Populärvetenskaplig sammanfattning

Elektromagnetism och speciellt elektromagnetiska vågor är grunden till nästan all modern trådlös överföring. Elektromagnetiska vågor kan liknas vid ljus och karakteriseras av frekvens, där endast ett fåtal frekvenser ger upphov till ljus som är synligt för människoögat. Mycket av den trådlösa överföringen som dyker upp i vardagen syftar till någon form av kommunikation, såsom WiFi, Bluetooth och 5G. Utöver kommunikation kan trådlös överföring även användas för att karakterisera en miljö, vilket ofta är syftet med radar. Precis som ljudvågor interagerar elektromagnetiska vågor med omvärlden och de reflekteras i objekt. Denna egenskap nyttjas av både fladdermöss och delfiner som använder sig av ljud för lokalisering, så kallad ekolokalisering. De genererar en ljudvåg som breder ut sig i miljön för att sedan lyssna efter reflektioner. Genom analys av reflektionerna får de information om objekten som gav upphov till dem. Grundtanken med radar är att nyttja samma fenomen som delfiner och fladdermöss gör, fast med elektromagnetiska vågor istället för ljudvågor. Grunden i analysen för såväl ekolokalisering som radar är fördröjningen till ekot. Både ljudvågor och elektromagnetiska vågor utbreder sig med en känd hastighet, och genom att mäta tiden mellan utropet och ekot kan man därför avgöra hur långt bort objektet befinner sig. Den stora skillnaden ligger i hur snabbt vågen utbreder sig, då elektromagnetiska vågor utbreder sig i ljusets hastighet som är ungefär en miljon gånger snabbare än ljudets hastighet. Analys av ekot kan även ge information om objektets hastighet genom att studera dopplerskiftet över tid, vilket följer ungefär samma princip som när ljudet av sirener låter annorlunda när en ambulans åker mot en gentemot när den åker bort från en.

I grunden bygger både kommunikationssystem och radarsystem på att en signal färdas från punkt A till punkt B. I ett radarsystem ligger punkt A och B ofta på samma plats medan de ofta är skilda i ett kommunikationssystem. Båda systemen använder information om vad som händer med signalen på vägen, men för väldigt olika syften. I ett radarsystem är inte signalen av något egenvärde och syftet är bara att studera förändringarna av den. I ett kommunikationssystem har dessa förändringar inget egenvärde men är användbara för att se till att meddelandet mottas så oförändrat som möjligt. Därför ser elektroniken i ett radarsystem och ett kommunikationssystem ofta olika ut då man optimerat dem för olika syften, men i princip är det inget som hindrar en från att kombinera dem. Mycket forskning har gjorts på, och görs fortfarande inom kombinerad kommunikation och miljökaraktisering, där man försöker kombinera dem på olika sätt. Ett exempel på hur detta kan användas är inom bilindustrin, där en bil kan kommunicera med en annan bil och samtidigt detektera reflektioner av radiosignalen och genom analys få information om den andra bilens hastighet och plats, vilket kan vara till nytta för exempelvis självkörande bilar eller liknande hjälpmedel.

Denna rapport redogör för konstruktionen och utvärderingen av ett sådant system som består av relativt billiga och lättillgängliga moduler och fritt tillgänglig mjukvara. Grunden i systemet är två så kallade mjukvarudefinierade radioenheter, vilka i princip är en kombinerad sändare och mottagare som kan ställas in med hjälp av en dator. En av dessa fungerar som radarsystemets sändare och skickar ut en signal med ungefär samma teknik som inom mobiltelefoni. Den andra agerar mottagare och tar emot ekot som behandlas på ungefär samma sätt som i ett traditionellt radarsystem. Till dessa kopplas två antenner av samma typ som brukade användas till TV mottagare, så kallade Yagi-Uda antenner, eftersom dessa ger en stark och tydligt riktad signal. Detta system används sedan för att undersöka om det finns några tydliga skillnader i hur väl radarn lyckas upptäcka bilar, cyklar och fotgängare när en klassisk radarsignal eller ett slumpat men känt meddelande skickas. Syftet med en sådan jämförelse är att se om det ger likvärdig prestanda om man skickar ett meddelande, vilket i så fall innebär att samma elektronik kan användas som både radar och kommunikationssystem samtidigt, vilket kan spara både plats och kostnad i produkter och öppna upp för mer effektiv användning av signalerna som skickas.

Acknowledgements

We would like to thank our academic supervisors, Fredrik Tufvesson and Michiel Sandra, as well as our supervisors from industry, for valuable feedback and guidance along the way. Furthermore, we would like to thank our fellow thesis workers for their contributions during the testing of the radar platform.

Table of Contents

Chapter 1

Introduction

Radars are typically associated with large-scale monitoring or detection endeavors that aim to track weather, detect aircraft and other vessels or to determine the velocity of a vehicle. It is however increasingly being used in such diverse scenarios as parking assistance in cars, occupancy monitoring of rooms and to allow for more directed transmissions in telecommunications.

These developments are taking place alongside trends of increasing inter connectivity of electronic devices and ever increasing flows of information in an increasingly crowded frequency spectrum. This combined with increased processing power have sparked interest in what has been termed WiFi sensing, where the communication channels from WiFi infrastructure is used to capture radar like data, and joint communication and radar that investigates the limitations of transmitting information at the same time as radar data is captured. The automotive industry has been a driving force in the latter as it allows for increasing coordination between vehicles, of great importance for autonomous vehicles. WiFi sensing on the other hand focuses on using existing communication infrastructure and protocols to extract further information from the environment, allowing for occupancy monitoring among other things.

Most modern communication systems currently utilize orthogonal frequency division multiplexing (OFDM) to transmit messages while many radars use a technique called frequency modulated continuous wave (FMCW) to transmit a relatively simple chirp to extract data about the surrounding area. Since OFDM is standard practice in wireless information transfer, it is a good starting point for a joint communication and radar system. In telecommunication the Zadoff-Chu sequence is often used for synchronization, and as it approximates an FMCW sequence it should be a suitable candidate for extracting radar data sent using an OFDM link. However, the Zadoff-Chu sequence does not contain any useful data, which is why a comparison with an arbitrary random data sequence is interesting, as it gives an approximate measure of the performance loss experienced when extracting radar data from a communication signal contra one optimized for sensing.

1.1 Purpose and aims

The overall purpose of this thesis is to investigate the performance of an OFDM modulated radar system at WiFi frequencies, constructed using commercially available devices. As such it will entail the design and evaluation of the feasibility of a radar system using low cost off-the-shelf communication equipment. Furthermore this thesis aims to experimentally evaluate the performance effects of allowing for joint communication and radar by transmitting a known randomly generated data sequence over an OFDM link and evaluating it against a Zadoff-Chu sequence. The Zadoff-Chu sequence approximates a typical FMCW chirp, and the random data is used to represent a communication packet. The performance will mainly be evaluated with respect to the ability to detect the distance and velocity of people and vehicles based on recorded measurement data. Thus the aim of the project is to construct a functioning radar platform from low cost software defined radios and readily available antennas and evaluate its performance experimentally, which could give useful insight for potential future endeavors in using existing communication infrastructure for joint communication and radar applications.

1.2 Method used to evaluate the purpose

In order to fulfill the purposes put forth, a short literature study is performed highlighting previous and related work in the field of joint communication and sensing, as well as how this thesis fits into that broader field. A theory section will detail the main theoretical background necessary to evaluate the performance and describe the key characteristics of the proposed radar platform. As the thesis aims to evaluate the performance of the proposed radar platform the system at hand will be described in depth and the component choices motivated in relation to the corresponding radar parameters. Some key aspects of the radar platform should be stated here as it relates to how the thesis is carried out. The setup will be based around two software defined radios (SDRs), two computers and two antennas. It features separate transmit and receive chains but no real time processing. The signals are generated and post-processed in each respective computer that is connected to the SDR via a USB 3.0 cable and interfaced using the open source tool GNU Radio [2]. Despite the onboard field programmable gate array (FPGA) chip allowing for real time processing it was decided against implementing it to limit the scope of the project, as an FPGA implementation would be a time consuming endeavor that is not integral to the purpose of this thesis. Thus the recorded data is processed in Python after it has been collected. Lastly, to evaluate the performance of the radar platform it is tested in different outdoor environments and with a variety of different target scenarios. In order to evaluate the feasibility of transmitting data simultaneously, each test will be carried out with a chirp signal as well as with a random data carrying signal, both transmitted using OFDM modulation.

1.3 Previous work

Joint communication and sensing has become a fruitful topic and a lot of previous work has been done in that broader field. This section will focus on a few related projects where a sensing setup has been constructed using SDRs as well as articles where OFDM modulated radars has been evaluated.

Measurements of wireless channels, also known as channel sounding, based on software defined radios has gained much popularity the last decade due to flexibility, portability, and cost-efficiency [22]. In [23] the design and implementation of a wideband distributed massive MIMO channel sounder for communication and sensing is presented. The channel sounder operates at 5-6 GHz with a bandwidth of 400 MHz and it is verified by two measurements in an indoor laboratory environment. An earlier version of the system is presented in [22]. It is a universal software radio peripheral (USRP) based channel sounder, developed as a proof-of-concept for other researchers seeking to build a channel sounder based on the USRP equipment. It is a ultrawideband single-input single-output (SISO) system with a custom signal processing block on the FPGA to limit the data stream.

Work has also been done on software defined radars. In [17] a 77-GHz software defined OFDM radar was developed and evaluated for automotive applications. It is configured as a SISO system with optimized performance by employing a peak-to-average power ratio reduction technique. The system was evaluated by two measurements in a semi anechoic chamber, one focusing on range and the other focusing on both range and Doppler. Other work related to OFDM radars have largely evaluated their performance using a simulation based approach. An example of this can be found in [5] where a traditional FMCW waveform is compared to an OFDM modulated waveform in automotive scenarios using simulations to allow for comparable parameters between the two. Another approach found in [6] is to theoretically compare the radar parameters in the case of OFDM in contrast to a frequency chirp where it is concluded that they can theoretically achieve the same performance though more signal processing is necessary in the OFDM case.

Chapter 2

Theory

Radar systems has evolved tremendously since their early days when their functions were limited to target detection and range determination. Modern radars are far more sophisticated as they can track, identify, image and classify targets while effectively suppressing interfering signals, both unwanted echos and jamming [20, p. 3]. Typical applications of radar ranges from military and civilian tracking of objects to mapping and monitoring of environment among many others [20, p. 3]. The basic working principle of a radar is that a radio frequency (RF) electromagnetic (EM) signal is transmitted towards a region of interest, the EM wave then propagates through and interacts with the environment and is reflected back from objects. Reflections, whether they are wanted or unwanted, are detected by the radar and processed for further analysis, usually to determine distance and velocity. Unwanted reflections are commonly referred to as clutter [20, p. 4].

The transmission and reception of the EM wave can either occur in the same physical location or in different locations, where the prior is classified as a monostatic system and the latter as a bistatic system [20, p. 18]. If the receiving and transmitting antennas are sufficiently close in a bistatic system, it can be considered as a monostatic system. So far only single-input single-output (SISO) systems have been considered, meaning only one channel for transmitting and one channel for receiving. By adding additional channels it is possible to create systems such as multiple-input single-output (MISO) or single-input multiple-output (SIMO) or a combination of both, multiple-input multiple-output (MIMO) [24]. Increasing the number of channels in a system results in a higher capacity for a given bandwidth and transmit power level, as well as improved spatial resolution, possibility to resolve direction and improved immunity to interference [24][19].

The EM waveforms used for radar can be divided into two main categories, namely modulated and non modulated, which can be transmitted as either continuous wave (CW) or pulsed. As the name continuous wave implies, an EM signal is transmitted continuously, usually without any interruptions while the receiver is on to detect reflections [20, p. 20]. On the other hand, for pulsed waveforms an EM signal of finite length is transmitted followed by a period where the transmitter is off and the receiver is on to detect reflections. Receiving whilst the transmitter is off is advantageous in monostatic systems, since the isolation between the transmitter and receiver is not perfect [20, p. 20].

Furthermore radar systems can be configured as non-coherent or coherent. For a non-coherent system only the amplitude of the received signal is measured, as opposed to a coherent system where the phase is measured in addition to the amplitude [20, p. 23]. All early radar systems were non-coherent, but most modern systems are coherent due to the additional information obtained from measuring the phase, such as motion characteristics [20, p. 23]. This thesis is focused on a monostatic coherent SISO CW radar although other techniques are considered for comparison. The following sections in this chapter provides further theory, concepts and tools used for the project.

2.1 The Zadoff-Chu sequence

As an approximation for a linear frequency chirp found in FMCW radars this thesis will use the Zadoff-Chu sequence that is commonly used as a synchronisation signal within communication. Zadoff-Chu is a complex-valued mathematical sequence with useful auto-correlation characteristics where the complex value at each position n of each Zadoff-Chu sequence $ZC\left(n\right)$ is given by

$$ZC\left(n\right) = \begin{cases} \exp\left(-j\frac{\pi n^2}{N_{ZC}}\right) & : N_{ZC} \text{ even} \\ \exp\left(-j\frac{\pi n(n+1)}{N_{ZC}}\right) & : N_{ZC} \text{ odd} \end{cases}, \tag{2.1}$$

where

$$0 \leq n < N_{ZC}$$

and N_{ZC} is the length of the sequence [29]. Some key properties are that the sequence is of constant absolute amplitude and it is periodic with period N_{ZC}. Furthermore, the auto-correlation of the sequence is non-zero only at one instant, which corresponds to the cyclic shift [29].

2.2 Software Defined Radio

Software defined radio is an accessible and versatile radio system where the implementation can be configured in software. A basic SDR system may consist of a personal computer preceded by a radio frequency front end. Radio frequency front end is a generic term that usually refers to all the circuitry between the antenna and mixer. In general for an SDR, the digitization at the receiver side can be performed at some stage downstream from the antenna, typically after down conversion, with a reverse process occurring for the transmit digitization [28, p.5].

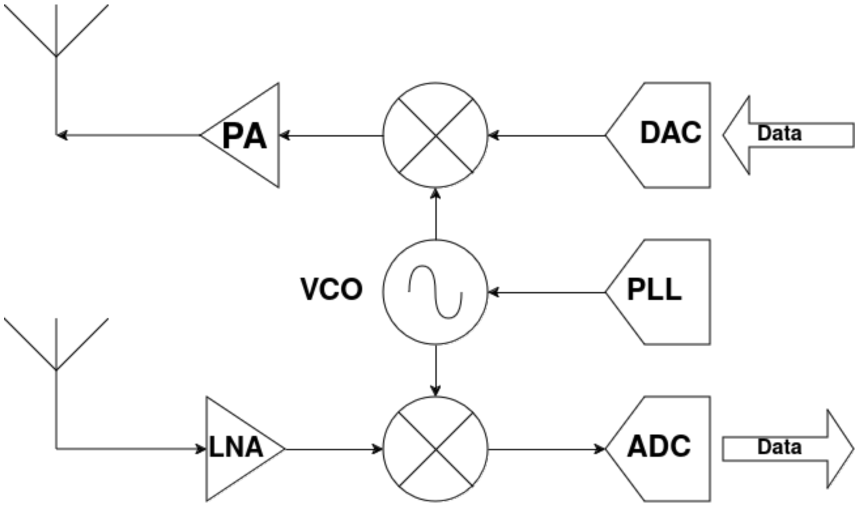

Figure 2.1: Simplified block diagram of a homodyne transceiver.

An example of a radio frequency front end is shown in Fig. 2.1 which illustrates a simple block diagram of a typical homodyne transceiver architecture. For the transmission side the in-phase (I) and quadrature-phase (Q) samples are fed to the digital to analog converter (DAC) and up-converted to radio frequency in the mixers. The now analog I and Q signals are combined and passed through the power amplifier (PA) to reach the antenna. For the receiver the inverse process occurs. The received signal passes through the low noise amplifier (LNA) to be down-converted to baseband I and Q signals. The baseband I and Q signals are digitized by the analog to digital converter (ADC) for further processing in the digital domain. The purpose of the voltage controlled oscillator (VCO) and the phase lock loop (PLL) is to generate the carrier signal. They are mentioned for completeness but will not be discussed further. Although Fig. 2.1 gives a good overview of a homodyne transceiver it is important for the reader to note that transceivers in general come in many different configurations. A transceiver can for instance have multiple amplification and filtering stages.

From a simple search of software defined radios on the web it is evident that there exists several types, ranging from cheap devices only capable of receiving, to high-end devices capable of multi-channel operation with high bandwidth and with configurable on-chip processing capabilities. A mid-range to high-end SDR can be described by the block diagram in Fig. 2.2 where the blocks are categorized to belong to either the RF front end or the digital back end, interfaced by the DAC and the ADC. In Fig. 2.2 digital signal processors (DSPs), general purpose processors (GPPs) and field programmable gate arrays (FPGAs) are mentioned as examples of components in the digital back end. As discussed an SDR enables a high level of flexibility since the implementation mainly is performed in software.

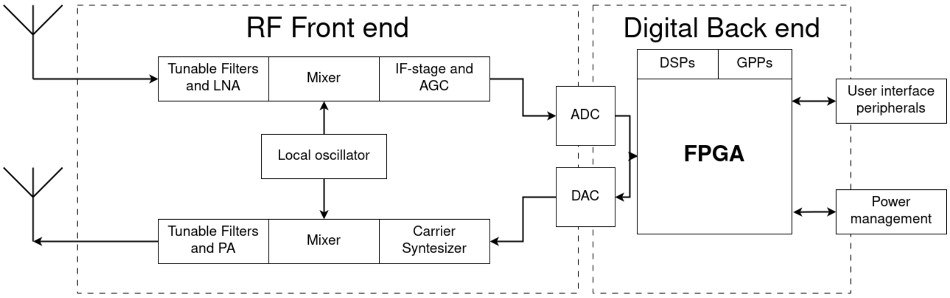

Figure 2.2: Basic hardware architecture of an SDR.

2.3 Introduction to the GNU Radio open-source toolkit

GNU Radio is an open-source software development toolkit for SDRs [2]. It is the core toolkit used in this thesis to interface with the SDR. GNU Radio Companion (GRC) provides a flowchart-like Graphical User Interface (GUI) for easier implementation. GRC comes with a variety of already implemented blocks, but in order to interface with the BladeRF it was complemented with the BladeRF source and sink blocks provided by Nuand [16]. In this way it is is possible to build an SDR system by connecting blocks in GRC to build a complete flowchart for transmission and reception of radio signals.

2.4 Peak-to-average power ratio and the crest factor

Peak-to-average power ratio (PAPR) is as the name implies a measurement of the relation between the peak and average power of a waveform, which can be expressed as

$$\text{PAPR} = \frac{P_{peak}}{P_{avg}}, \tag{2.2}$$

where P_{peak} is the peak power and P_{avg} is the average power of the waveform. Another method for quantifying this relation is through the crest factor (CF), which is the relation between the peak value and the effective value of a waveform, which can be expressed as

$$\text{CF} = \frac{V_{peak}}{V_{rms}} = \sqrt{\text{PAPR}}, \tag{2.3}$$

where V_{peak} is the largest absolute value of the waveform and V_{rms} is the root-mean-square value [9]. The CF for complex signals x can be analyzed according to

$$\text{CF} = \frac{V_{peak}}{V_{rms}} = \frac{\max\left(|x|\right)}{\sqrt{\text{mean}\left(|x|^2\right)}}. \tag{2.4}$$

2.5 Introduction to the FMCW- and the OFDM technique

As this thesis aims to investigate radar by OFDM another radar technique is presented for reference, namely the FMCW technique which is a common way of implementing radar systems.

2.5.1 FMCW

Frequency modulation continuous wave is a common technology for radar applications. Provided a center frequency f_c and bandwidth B, a transmit signal is constructed by the modulation of frequency over time within the bandwidth B, as illustrated in Fig. 2.3. A simple modulation scheme is linear modulation which is commonly referred to as a linear chirp. The linear chirp can for instance be generated by starting with a frequency of $f_c - \frac{B}{2}$ and linearly increase the frequency up to $f_c + \frac{B}{2}$. Continuous wave is achieved by repeatedly transmitting these chirps. As the signal interacts with the surroundings it is attenuated and reflections from objects are received. The reflected signals can be processed to obtain information about the objects such as their distance and radial speed with respect to the radar. Although FMCW can be used with varying transceiver architectures, it is commonly implemented such that the beat frequency f_b is the output of the mixer as the transmitted chirp is mixed with the received chirp. This concept is illustrated in Fig. 2.3a. The beat frequency is the difference in frequency between the RF output and input and can be expressed as

$$f_b = \frac{df}{dt}\frac{2R}{c}, \tag{2.5}$$

where df/dt is the slope of the chirp, c is the speed of light and R is the range to the target that generated the reflection [21]. By rearrangement of (2.5) it is evident that the range is proportional to the beat frequency according to

$$R = \frac{f_b c}{2(df/dt)}. \tag{2.6}$$

Since the speed of light is a constant and the slope is a design parameter, calculating the range is simply a matter of determining the beat frequency. It is of importance to note that the preceding result presupposes a transceiver architecture that enables extraction of the beat frequency. For other transceiver architectures such as homodyne, an alternative approach can be taken to calculate the range. By measuring the round-trip time of the electromagnetic wave, the range R can be determined as

$$R = \frac{c\Delta T}{2}, \tag{2.7}$$

where ΔT is the time delay, commonly determined by counting the number of ADC clock pulses that occur between the transmit time and target time [21, p.30].

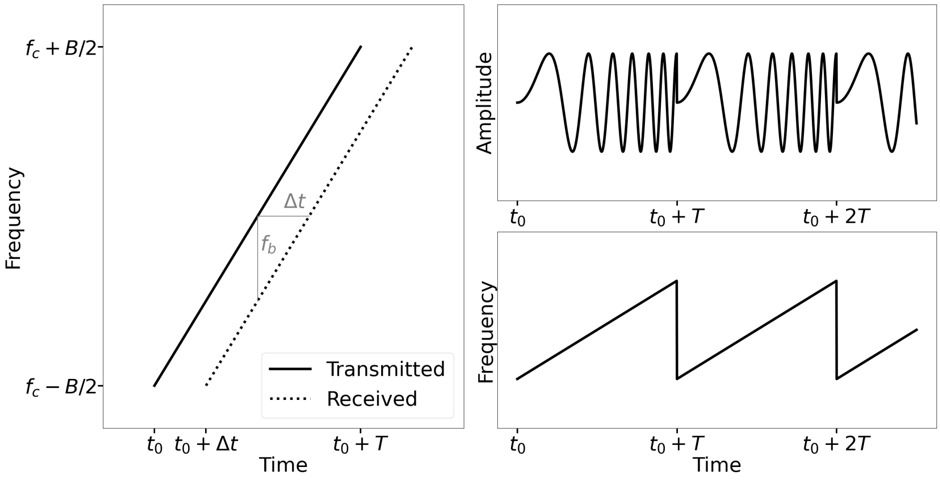

(a) Transmitted and received chirp.

(b) Consecutive chirps.

Figure 2.3: Illustration of FMCW.

2.5.2 OFDM

Orthogonal Frequency Division Multiplexing is a type of modulation scheme commonly used within telecommunications [26, p. 6]. OFDM was developed to allow for higher bit rates and bandwidths by mitigating the problem of inter-symbol interference. This is achieved by parallelization of the serial data stream and thus increasing the symbol time while maintaining the bit rate, which in turn lowers the risk of a multi-path component interfering with the symbol. The parallelization is done by dividing the available bandwidth into several narrower segments that each carry data thus allowing a whole segment of the data stream to be sent at the same time [25, p. 130]. Each of these segments are modulated separately and are typically referred to as sub-carriers [25, p. 130]. If nothing was done to the sub-carriers they would run the risk of bleeding into one another unless ample frequency spacing was put between them, however this would limit the bandwidth. The orthogonality in OFDM is used to overcome this, by placing each sub-carrier orthogonal to the others they are uncorrelated and at the peak of each sub-carrier all others will have a zero crossing instead [1, pp. 205–207]. To ensure that the sub-carriers are orthogonal to each other the frequency spacing Δf is set according to

$$\Delta f = \frac{1}{T_s}, \tag{2.8}$$

where T_s is the transmit period. It should be mentioned that OFDM is foremost a multiplexing scheme rather than an actual modulation scheme as the sub-carriers are commonly modulated using QAM, QPSK, BPSK or other modulation schemes [1, p. 221]. There is one major drawback to using OFDM modulation, and that is the poor PAPR due to the signal consisting of multiple uncorrelated narrow band signals in the time domain. At random these narrow band signals will add constructively causing high peak powers while the average power remain rather low [1, p. 210]. This cause problems both at the transmitter and receiver as the components need to handle the peak power while the system normally work with the average power. This is most evident in the power amplifiers that either waste a lot of power to accommodate the high peak amplitudes, causing low efficiency, or operate at higher efficiency but clipping the peaks [1, p. 211]. Furthermore, due to the longer symbol times, OFDM signals are very sensitive to frequency offsets, which cause the received signal to be sampled off peak, leading it to be both weaker and lose a lot of the advantages gained by orthogonality, causing catastrophic inter channel interference [1, p. 210]. This could cause a problem in a bistatic radar scenario as two commercial oscillators will differ somewhat regardless of whether they have the same nominal frequency [1, p. 209].

In the carrier allocation it is common to separate the carriers into three categories, namely data-, pilot- and null-carriers. Pilot-carriers are designated for transmitting symbols known to both the transmitting and receiving unit, in order to extract information about the wireless channel. Data-carriers transmit the actual data, hence it is only known by the transmitting unit. Null-carriers are designated to create a headroom between occupied bandwidth (OBW) and signal bandwidth (BW). The OFDM baseband signal is commonly generated by the inverse discrete Fourier transform (IDFT) and the total number of carriers is determined by the length of the IDFT. The relation between the carrier types can be described as

$$f_{samp} = \mathrm{BW} = N\Delta f > K\Delta f = \mathrm{OBW}, \tag{2.9}$$

where N is the length of the IDFT, K is the sum of pilot- and data-carriers and Δf is the frequency spacing between carriers [3]. Hence, the number of null carriers is $N - K$ and the ratio OBW/BW is the same as the ratio K/N.

2.6 Some key performance parameters of a radar system

Fundamentally all radar systems follow the radar range equation (RRE) which can be expressed as

$$P_r = \frac{P_t G_t G_r \lambda^2 \sigma}{(4\pi)^3 R^4}, \tag{2.10}$$

where P_r is the received power, P_t is the transmitted power, λ is the wavelength, R is the distance to the target, G_t and G_r is the antenna gain of the transmitting and receiving side respectively and σ is the radar cross section [20, p.64].

The radar cross section (RCS), can be viewed as a measure of the targets size as seen by the radar and is defined as

$$\sigma = \lim_{R\to\infty} 4\pi R^2 \frac{|E^{scat}|^2}{|E^{inc}|^2}, \tag{2.11}$$

where E^{scat} is the electric field scattered by the target in a given direction after being illuminated by E^{inc}, the electric field incident on the target [21, p. 219]. An

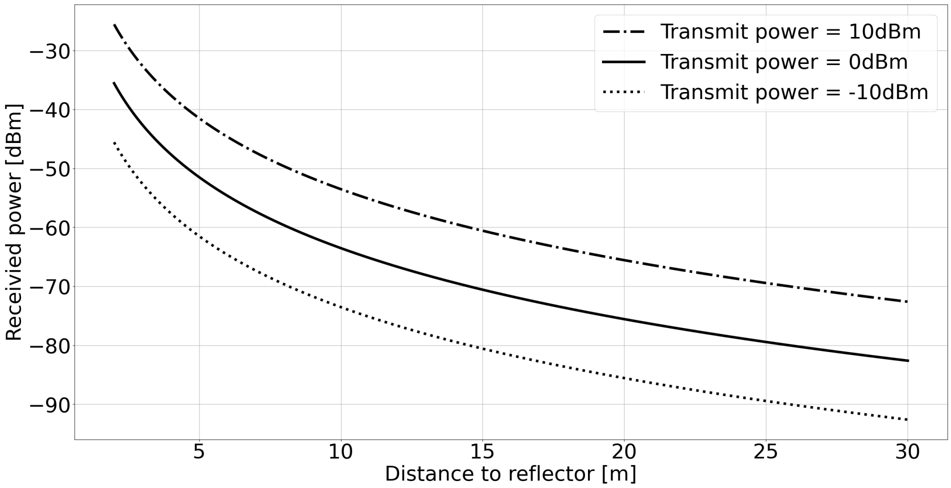

Figure 2.4: Illustration of (2.10) for three different transmit power levels where P_r is a function of only the distance R, where $G_t = G_r = 18$ dBi, $\lambda = 0.12$ m and $\sigma = 3.74$ m², corresponding to the reflector used in the tests.

illustration of the behavior of the radar range equation is shown in Fig. 2.4. In addition to the general RRE, the performance of a radar system can be evaluated more precisely in multiple ways and some key parameters are presented in the following part of this section. The range resolution ΔR is given by

$$\Delta R = \frac{c}{2B}, \tag{2.12}$$

where c is the speed of light and B is the bandwidth [21, p. 36]. As discussed in [21, p. 36] if a Hann, Hamming or similar windowing function is used, (2.12) becomes

$$\Delta R = \frac{1.3c}{2B}. \tag{2.13}$$

Another limiting factor is the sampling frequency at the receiver side, as it determines the bin size ΔR_{samp} according to

$$\Delta R_{samp} = \frac{c}{2f_s}, \tag{2.14}$$

where f_s is the sampling frequency and the factor "two" in the denominator is to account for the round-trip time of the electromagnetic wave. In the case that null-carriers are used for the OFDM signal the expression for ΔR_{samp} has to be adjusted to

$$\Delta R_{samp} = \frac{c}{2f_s}\frac{N}{K}, \tag{2.15}$$

where N is the number of sub-carriers, and K is the number of occupied sub-carriers. Furthermore, for an OFDM radar system the number of sub-carriers defines the maximum unambiguous range R_{max} for a given bandwidth as

$$R_{max} = \frac{cN}{2B}, \tag{2.16}$$

where N is the number of sub-carriers [17]. In addition to the range resolution and the maximum unambiguous range, the velocity resolution ΔV and the maximum unambiguous velocity V_{max} can be defined as

$$\Delta V = \frac{c}{2nf_c\text{PRT}}, \tag{2.17}$$

$$V_{max} = \pm\frac{c}{4f_c\text{PRT}}, \tag{2.18}$$

where n is the number of pulses, f_c is the carrier frequency and PRT is the pulse repetition time [17].

2.7 Signal Processing

Due to the nature of wireless signal transfer, the received echos will be heavily attenuated and thus of small magnitude when it reaches the receiver. This makes it vulnerable to cross-talk as well as noise which risk masking the echo entirely, thus necessitating the use of signal processing to maximize the likelihood of detection. Since the transmitted signal is OFDM modulated, the signal processing at the receiver can be categorized into two main parts, one which demodulates the signal and one that that aims to differentiate the echo from the rest of the received signal. The following section will start with a short description of typical signal processing in radar applications, then describe the demodulation procedure before finally highlighting some signal properties.

2.7.1 Radar signal processing

When recording radar data it is usually saved in a data frame, often times called a data cube if several Tx and Rx channels are used. The data frame is usually saved in a matrix where one dimension consists of the range bins or samples in the transmitted sequence and the other dimension of each received sequence in chronological order. These dimensions are usually referred to as fast-time and slow-time respectively [21, p. 502]. Each sample thus correspond to a specific sequence number and range bin and consists of both the I and Q component of that sample [21, p. 502]. The length of the slow-time dimension constitutes the coherent processing interval and is a snippet of the recording with subsequent sequences coherent with each other [21, p. 502]. The range is determined on each chirp while an FFT performed on each range bin across all sequences is performed to yield information in the Doppler domain [21, p. 503].

2.7.2 Demodulation

At the receiver side in an OFDM system the aim is to serialize the received signal and demodulate the data. This process involves multiple stages which partly includes synchronization and removal of the cyclic prefix. However since this thesis handles OFDM for radar application simplifications of the processing at the receiver side are possible. Most noteworthy is that no synchronization is performed at the time of receiving and cyclic prefix is not used, which simplifies the implementation of the receiver side.

2.7.3 Signal properties

The received signal is presumed to be the superposition of echoes, the antenna leakage, as well as noise. Furthermore the different components of the signal are assumed to be independent of one another as any echoes themselves should not be influenced by the antenna leakage despite them stemming from the same transmitted signal.

The signal processing put in place to differentiate the echo can be broadly summed up as two separate steps, averaging, and normalising with a calibration signal. Averaging assumes that the noise has a mean value of 0 while any echo will have a non zero mean, thus averaging over each point should bring down the noise floor while leaving any echos intact.

Due to the vast difference in distance traveled between the echoes and the antenna leakage the leakage signal is likely to make up the largest portion of the received signal. The normalisation is put in place to remove the effect of the leakage signal from the received signal. As discussed in [18, p. 82] the received signal $y(n)$ can be described as the convolution of the transmitted signal $x(n)$ and the channel impulse response $h(n)$ according to

$$y(n) = x(n) * h(n). \tag{2.19}$$

In the context of radar, the impulse response $h(n)$ is of great interest since it can give the delay of the echo in terms of samples. Though the impulse response is of primary interest applying the discrete Fourier transform simplifies the calculations of it. Thus (2.19) is transformed to

$$Y(f) = X(f) \cdot H(f). \tag{2.20}$$

Rearranging (2.20) yields the system transfer function $H(f)$ as

$$H(f) = \frac{Y(f)}{X(f)}. \tag{2.21}$$

The IDFT is applied to (2.21) to yield the system impulse response

$$H(f) \xrightarrow{\mathscr{F}^{-}} h(n). \tag{2.22}$$

Furthermore, the convolution operation is both associative and distributive [18, pp. 83–85], thus satisfying

$$[x(n) \circledast h_1(n)] \circledast h_2(n) = x(n) \circledast [h_1(n) \circledast h_2(n)], \tag{2.23}$$

and

$$x(n) \circledast [h_1(n) + h_2(n)] = x(n) \circledast h_1(n) + x(n) \circledast h_2(n). \tag{2.24}$$

Thus if the received signal is a superposition of several echoes it will assume the form

$$y(n) = x(n) \circledast h_1(n) + x(n) \circledast h_2(n) + ... + x(n) \circledast h_k(n). \tag{2.25}$$

2.8 Antennas

The gain of the antenna is defined by its directive gain, i.e. how the radiated energy is distributed in relation to an isotropic radiator with the same radiated power, as will be denoted by the use of dBi when discussing antenna gain. The directive gain in the center of the main lobe is called directivity [11, p. 43] and will be denoted D_0. As stated in [11, p. 56] the directivity combined with the polarization efficiency e_{pol} and total radiation efficiency e_{rad} gives the total antenna gain G_0 as

$$G_0 = e_{rad} e_{pol} D_0. \tag{2.26}$$

The total radiation efficiency is in turn defined as

$$e_{rad} = e_r e_{abs} = (1 - |\Gamma|^2) e_{abs}, \tag{2.27}$$

where Γ denotes the reflection coefficient and e_{abs} regards ohmic losses [11, p. 57]. As discussed in [11, p. 57] the polarization efficiency e_{pol} is given by

$$e_{pol} = \left(\frac{E(0^\circ, 0^\circ) \cdot \hat{co}^*}{|E(0^\circ, 0^\circ)|} \right)^2 . \tag{2.28}$$

Different antenna types naturally have different directivity characteristics. This thesis will mainly concern the Yagi-Uda antennas and patch antennas, but to a small extent also monopoles. The main difference between these is that the patch and Yagi-Uda are directive antennas [10, 248 and 322], that is, they send out a beam of energy in the direction they are pointed. The monopole on the other hand is omnidirectional, meaning that it radiates all around its z-axis [10, p. 58]. Furthermore all the antenna types mentioned are linearly polarized [10, pp. 58, 246, 322]. They do however differ in regard to directivity. Monopoles typically has a directivity of 5.2 dBi or 6.8 dBi depending on whether it is a quarter wavelength or half wavelength [10, p. 192]. The typical patch antenna has a maximum directivity of about 6 dBi broadside to the antenna [10, p. 324] and a rather broad beam with a beam width of about 65 degrees [4, p. 51]. The directivity of the Yagi-Uda antennas depend on the amount of directors and reflectors added, generally more parasitic elements increase the directivity [33, p. 639].

Chapter 3

Methodology

The main goal of this thesis is to investigate how a radar system can be implemented using software defined radios and how the system performance is affected by a data carrying signal in relation to a chirp-like signal. To carry out this investigation this thesis relies on a radar system consisting of two software defined radios from Nuand, of the model BladeRF xA9, two Yagi-Uda antennas designed for use with 4G signals, a signal generator created in Python, a signal processor created in Python and the open source software GNU Radio with Nuands own transmit and receive blocks installed to interface between the computers and the software defined radios. To assess the performance of the system, field tests are carried out where one SDR is used to transmit, one to receive and a docking station or dongle to allow for USB 3.0 data transfer. Most of these tests were carried out in different outdoor environments.

The following sections will describe and motivate how the proposed radar system is implemented, covering the entire link from signal generation to processing of the received signal. The chapter is split into a few major components centered around different aspects of the system. First there will be a discussion centered around the SDR units, this will be followed by a segment about the transmitted signal and how it is generated. A discussion of the antennas utilized and how it affects the choice of frequency follows and the chapter then ends with a section about the signal processing applied to the received signal.

3.1 Design and implementation of the radar system

One of the major difficulties in building a radar system from communication hardware such as SDRs is the fixed nature of the radio front end. By design the nature of this thesis is largely investigative, meaning that there were no given specifications for performance. The following sections will discuss the choice of SDRs

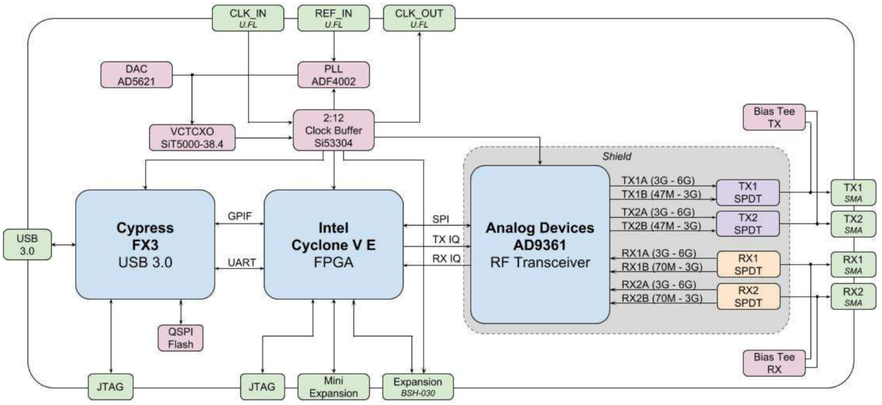

Figure 3.1: Schematic of the BladeRF 2.0 micro xA9 [15].

and how these are configured based on limitations in both hardware and software, stemming mainly from signal leakage between the Rx-channel and Tx-channel on the SDR unit, synchronisation and the inability to extract beat frequency due to a homodyne receiver structure. Furthermore, limitations stemming from the interfacing between the SDRs and the computers are briefly discussed, as is the division of tasks between GRC and Python.

3.1.1 The choice of SDR - BladeRF 2.0 micro xA9

For this thesis it was decided to use the BladeRF 2.0 micro xA9 SDR. It is a relatively powerful SDR with features such as full-duplex capability. Since this thesis is conducted as an investigation, the requirements of the system is not known beforehand, hence it was convenient so pick an SDR that provides flexibility. Furthermore, it comes with clock synchronization capabilities which for radar applications is crucial when using multiple units. The BladeRF is based on the AD9361 2x2 transceiver with Rx and Tx bands up to 6 GHz and a direct conversion architecture. It comes with the Cyclone V, which is a capable FPGA. The overall computing power onboard is however not the main concern as the thesis aims to investigate OFDM rather than optimizing general performance. Consequently, a provided FPGA-image is used and the baseband samples are streamed over the USB 3.0 interface without additional on-chip processing. The schematic of the BladeRF can be seen in Fig. 3.1.

3.1.2 Investigation of the hardware

At an early stage it was concluded that the isolation between the transmitting and receiving channels on one BladeRF is low. The method used to quantify and compare the isolation between channels is based on terminating the Tx-channel of interest with a 50 Ω dummy load and transmitting a known signal. Simultaneously the data is received by the Rx-channel of interest. With known Tx and Rx data, the transfer function is calculated and ultimately used as a measurement of isolation. Using two BladeRF units, one for transmitting and one for receiving, improved the isolation as the units can be separated by an arbitrary distance. The transfer functions using one and two BladeRF units are shown in Fig. 3.2. However, by using two separate units the benefit of synchronized transmitter and receiver operation is lost. Fortunately the BladeRF is capable of both outputting its clock and receiving an external clock. By having one BladeRF output its clock to another BladeRF, frequency synchronization is achieved. Connecting the Tx1 port of the respective BladeRF units to an oscilloscope and transmitting identical signals yields the results pictured in Fig. 3.3. The pattern seen in Fig. 3.3 was constant over the entire period of a few minutes it was observed. Additionally, it is clear that there is a phase shift between the signals, indicating that the signals are not synchronized in time, which is another consequence of using multiple BladeRF units. The phase shift appears to be random for every start of a new transmission, but the frequency synchronization ensures that the phase error remains constant during the period of operation.

From the investigation of isolation and synchronization it is concluded that the main tradeoff for using two BladeRF units is the absence of synchronization in time, for significantly improved isolation between Tx1 and Rx1. Since the system simultaneously transmits and receives signals, a portion of the transmitted signal will leak directly from the Tx-side to the Rx-side. This leakage is usually undesired since it can be of significant magnitude and deteriorate the performance of the radar system, hence great effort is usually invested in minimizing it. However, it is in signal processing possible to take advantage of the leakage to perform a rough synchronization in time, since it will always be present as the first signal of sufficient magnitude to reach the Rx-side. For these reasons it was concluded that the improved isolation is more critical than ensuring time synchronization, hence separate BladeRF units are used for transmitting and receiving. Using separate units for transmission and reception has the added benefit of dividing the workload between two systems with separate communication busses. Consequently it is possible to operate the Tx-side and Rx-side from different computers.

3.1.3 Interfacing with the BladeRF

The BladeRF comes with a USB 3.0 interface which has a theoretical maximum transfer speed of 5 Gbit/s. Two laptops are used to connect to the BladeRF units, that are only equipped with USB 2.0 and USB C ports, with maximum transfer

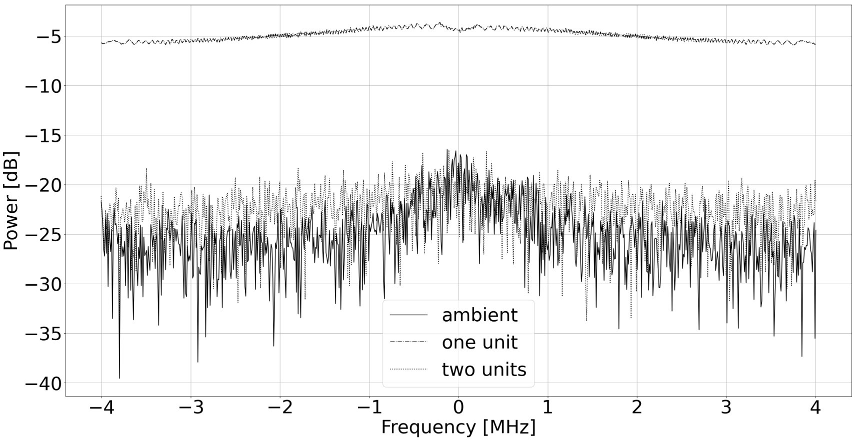

Figure 3.2: Tx1-to-Rx1 transfer function with a 50 Ω termination on the Tx1 port and the Rx1 port open-circuited. Thus there are no antennas connected. One unit concerns the transfer function between Tx1 and Rx1 on the same BladeRF unit while two units regard the transfer function between the Tx1 and Rx1 port on separate units. The two units are separated by 240 mm. In the ambient transfer function Tx1 is idle. The average of the transfer function for one unit, two units and ambiance are -4.9 dB, -22.0 dB and -24.0 dB respectively.

speeds of 480 Mbit/s [30] and 5 Gbit/s or 10 Gbit/s depending on what USB 3 protocol it uses [31]. As the baseband data is streamed between the BladeRF and the computer, it puts a lot of stress on the data buss, depending on how the radar system is configured. The BladeRF supports sampling speeds of up to 122.88 Msps with an 8 bit sample format. The resulting maximum transfer speed is

$$122.88 \cdot 10^6 \cdot 8 \cdot 2 \approx 1966 \text{ Mbit/s},$$

as there are both an I and a Q part. As a result of the large amount of streamed data, the data bus proved to be a limiting factor when increasing the sampling speed of the system. Accordingly, separate computers were almost exclusively used for operating the Tx- and Rx-side to avoid having both the Tx- and Rx data streamed over the same bus. Despite separating the streams, the data bus still proved insufficient for reaching the maximum sampling speed.

3.1.4 Physical setup

In order to ensure that the measurement setup is constant each measurement and to protect the equipment a simple fixture was constructed. The fixture consists of a plastic board and two racks to mount each SDR vertically with a fixed spacing between them on the board. This is the main function of the fixture as the signal

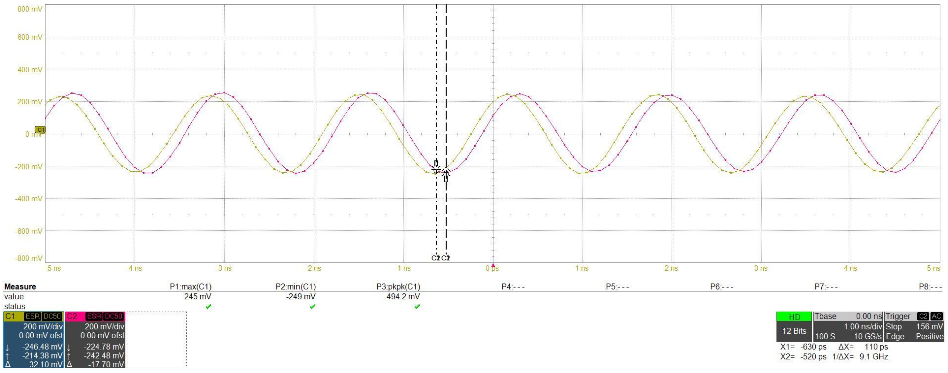

Figure 3.3: Tx1 on two separate BladeRF units with synchronized clocks.

leakage is dependent on the physical separation of the units. Lastly there is the antenna mount, there is a 3D printed mount for patch antennas at the front end of the board. However since Yagi-Uda antennas are used in the final implementation the relevant antenna mount is rather a separate improvised cardboard fixture holding both antennas. As with the SDR racks, the main objective of the antenna mount is to ensure constant interference behavior between the antennas. The setup is illustrated in Fig. 3.4 and was largely constructed of materials with low dielectric constants to minimize its interaction with the transmitted signals and leakage.

3.2 OFDM transmission and reception

This chapter presents an overview of how data is transmitted and received over OFDM. The signal generation, transmission and reception are presented as well as initial processing of the received signal.

3.2.1 Generation of the OFDM signal

For simplicity the transmit signal is generated in Python using standard modules. There are two main design variables to decide when generating the signal, the number of sub-carriers N and the number of occupied sub-carriers K. From (2.9) it is evident that for a given sample frequency the choices of N and K will determine the frequency spacing of the sub-carriers Δf, as well as the occupied bandwidth (OBW), which is the ratio K/N multiplied with the sampling frequency. To best describe the allocation process a vector $\vec{v}$ of length N is introduced, representing frequency bins with initial values of 0. The mapping of the data sequence starts at index $N - K/2$ and ends at index $K/2$ after wrapping around and skipping

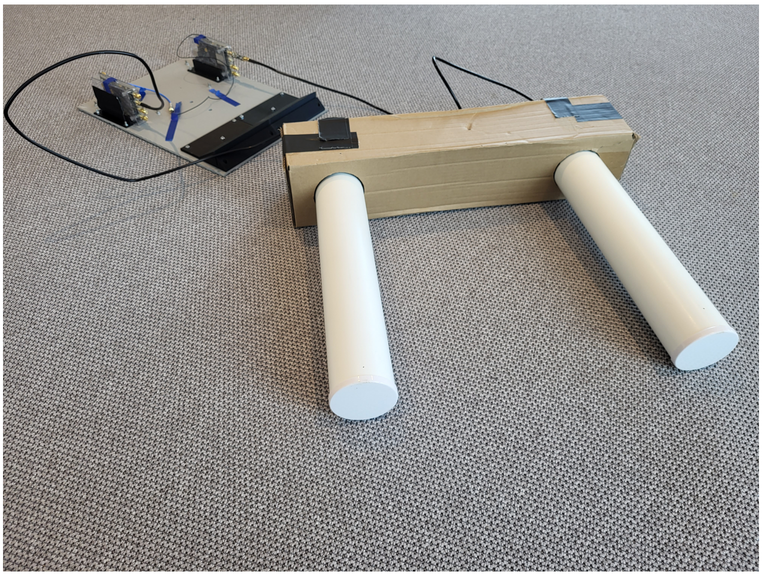

Figure 3.4: The physical radar setup.

index 0. The result is a data allocation at both negative and positive frequencies centered around the non-allocated DC-carrier. Additionally there are $N - K - 1$ null-carriers centered around the Nyquist frequency creating a headroom around the Nyquist frequency. An example of the allocation can be seen in Fig. 3.5.

The carrier allocation is followed by the IFFT to generate the baseband transmit signal. To ensure optimal performance of the DAC on the BladeRF, the signal is scaled such as the largest amplitude of the signal is 0.85. This is because substantial distortion in the signal was observed for values close to and above 1. Lastly the scaled baseband signal of length N is saved to a binary file ready for transmission.

3.2.2 The transmission and reception process of OFDM

The transmission and reception is done in GNU Radio Companion (GRC). The generated baseband transmit signal is loaded into GRC and streamed repeatedly to a BladeRF for transmission. Simultaneously the other BladeRF streams samples of received data which is saved to a binary file. All system parameters are set in GRC such as carrier frequency, sample rate, bandwidth and gain for both the transmitter and the receiver side. The GRC flow-graph is shown in Fig. 3.6. The main constraint when deciding for system parameters is following regulations for transmission. Consequently 2.45 GHz, the center of the 2.4 to 2.5 GHz ISM-band, is used as the center frequency for the radar system. Furthermore a maximum bandwidth of 100 MHz should not be exceeded.

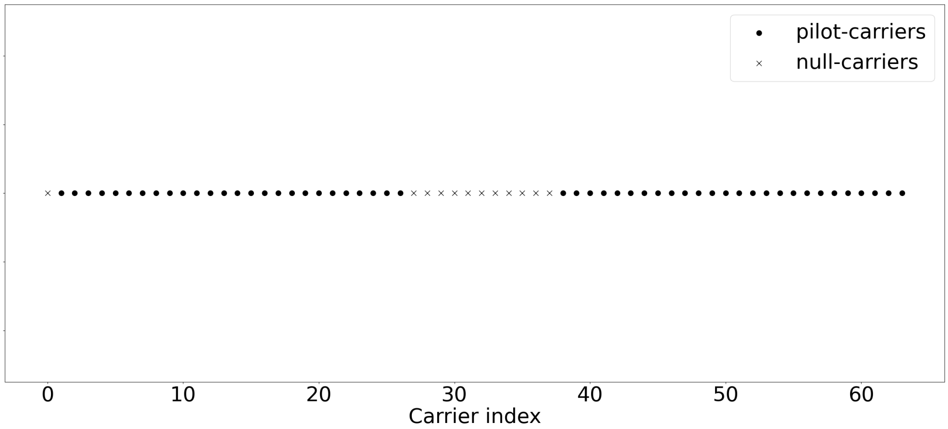

Figure 3.5: Example of carrier allocation for $N = 64$ and $K = 52$. Dots are indices of pilot-carriers and crosses are indices of null-carriers.

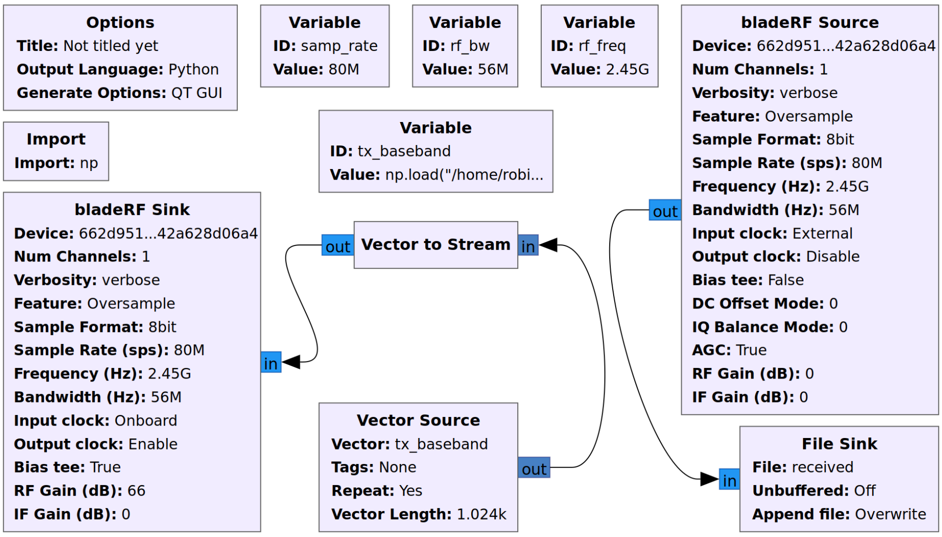

Options
Title: Not titled yet
Output Language: Python
Generate Options: QT GUI

Variable
ID: samp_rate
Value: 80M

Variable
ID: rf_bw
Value: 56M

Variable
ID: rf_freq
Value: 2.45G

bladeRF Source
Device: 662d951...42a628d06a4
Num Channels: 1
Verbosity: verbose
Feature: Oversample
Sample Format: 8bit
Sample Rate (sps): 80M
Frequency (Hz): 2.45G
Bandwidth (Hz): 56M
Input clock: External
Output clock: Disable
Bias tee: False
DC Offset Mode: 0
IQ Balance Mode: 0
AGC: True
RF Gain (dB): 0
IF Gain (dB): 0

Import
Import: np

Variable
ID: tx_baseband
Value: np.load("/home/robi...

bladeRF Sink
Device: 662d951...42a628d06a4
Num Channels: 1
Verbosity: verbose
Feature: Oversample
Sample Format: 8bit
Sample Rate (sps): 80M
Frequency (Hz): 2.45G
Bandwidth (Hz): 56M
Input clock: Onboard
Output clock: Enable
Bias tee: True
RF Gain (dB): 66
IF Gain (dB): 0

Vector to Stream

Vector Source
Vector: tx_baseband
Tags: None
Repeat: Yes
Vector Length: 1.024k

File Sink
File: received
Unbuffered: Off
Append file: Overwrite

Figure 3.6: Flow-graph in GRC used for transmission and reception of the OFDM signals. For separate systems for the transmission and reception, the flow-graph is split so that only the transmission blocks or reception blocks are used in the corresponding system.

3.2.3 Initial processing of the received OFDM signal

The received baseband samples are loaded into Python for analysis. To get the received data sequence initial processing is performed by taking the FFT of the signal followed by serialization of the data. The serialization of the data is the inverse of the carrier allocation operation.

3.3 The various data transmitted over OFDM

As mentioned in section 2.5.2 it is common to talk about data-, pilot- and null-carriers in an OFDM communication system. As these systems strive for high throughput it is desirable to maximize the number of data-carriers, hence minimizing the number of pilot-carriers. At the receiver side pilot-carriers are used to estimate the channel by interpolation. The estimated channel can be used to perform equalization of the received data to compensate for the effect of the channel. For radar applications the aim is to extract the channel state information (CSI). Therefore interpolation of the channel should ideally be avoided for accurate CSI. This is achieved by only having pilot- and null-carriers in the system. The best radar performance is therefore obtained by excluding data-carriers, which is the approach taken.

3.3.1 The Zadoff-Chu sequence as data

As the CSI is optimized by not having any data-carriers it is now a matter of deciding what data to send on the pilot-carriers. This is where the properties of the Zadoff-Chu sequence in section 2.1 are convenient. Since the sequence is complex with constant amplitude, data points are located on the perimeter of a circle in the complex plane, which results in a low crest factor. Once the OFDM parameters N and K are decided, a Zadoff-Chu sequence is generated of length $K+1$ according to (2.1). K is ideally chosen so that $K+1$ is odd. The reasoning for $K+1$ being odd is that it is convenient in the carrier allocation process since the middle point of the sequence can be mapped to the DC-carrier and overwritten as a null-carrier. Consequently the received sequence will be of length K and in order to process the signal, linear interpolation around the DC-carrier is performed to recover a length of $K+1$. This approach is discussed in further detail in [14] and adopted in this thesis.

3.3.2 Digitally modulated sequences as data

The purpose of sending digitally modulated sequences as data is to better represent what is done in communication systems, where techniques such as quadrature amplitude modulation (QAM) and phase shift keying (PSK) are utilized. To generate a digitally modulated data sequence, a random sequence of bits is first generated. The length L of the bit sequence is determined by

$$L = K\mu \tag{3.1}$$

where K is the number of symbols and μ is the number of bits per symbol. The bits are drawn from the Bernoulli distribution with $p = 0.5$, resulting in equal probability of 0 and 1. The symbols are generated from the random bit sequence by a mapping table corresponding to the applied modulation technique. Generation of the sequence is done once, so that it is always the same and known when used.

3.4 Antennas

Several choices of antennas were tested on the system, initially patch antennas were utilized, however the final setup use two Yagi-Uda antennas instead due to their superior directivity and thus higher antenna gain. In this application, when both the transmitter and receiver are active simultaneously, the leakage will set the gain level of the automatic gain control (AGC) in the receiver and thus there is a risk that small echoes goes undetected due to them being outside of the dynamic range of the system. This causes the beam width and antenna gain to be important parameters since they influence the size of the echo in relation to the leakage. However this also causes bandwidth and matching to become of importance as they influence the realized antenna gain.

The Yagi-Uda antennas used in the radar platform has a peak directivity of 18 dBi, with an error margin of ±1 dBi and a beamwidth of 30 degrees as specified in its data sheet [32]. This is preferred over the patch antennas that could be expected to produce a directivity of 6 dBi as presented in section 2.8, 12 dB lower than the Yagi-Uda, while giving a much broader beam. Thus the Yagi-Uda antennas are expected to produce a total gain in the system that is about 24 dB higher than if the patches are utilized. The Yagi-Uda antennas however needed to be modified to achieve this as they came with 10 m cable of the type LMR-195 [32]. This cable type has an attenuation of 55.4 dB/100 m at 2.5 GHz [12], meaning the cable would cause about 5.5 dB attenuation at each end for a total of 11 dB in the system, negating a portion of the benefit of using the Yagi-Uda antennas. To solve this the antenna cables were desoldered from the driven element, shortened to about 1 m, recrimped and resoldered to the driven element. The two Yagi-Uda antennas were placed in a rather ad-hoc holder made out of cardboard, shown in Fig. 3.7a, to ensure they had the same relative position in all tests.

Since the Yagi-Uda antenna is linearly polarized the two antennas were placed side by side such that their respective folded dipoles were oriented in the same manner as seen in Fig. 3.7b to eliminate any unnecessary polarization losses that would lower the antenna gain in accordance to (2.26). Furthermore the S11 and S22 parameters were measured in a vector network analyzer to find the frequency

(a) Yagi-Uda antennas with radome. **(b)** Yagi-Uda antennas without radome.

Figure 3.7: Antenna setup.

with the lowest reflection coefficient for each antenna. This measurement is shown in Fig. 3.8a.

Fig. 3.8a shows that the largest negative peak, corresponding to the lowest reflection coefficient and thus smallest losses according to (2.27) is to be found at about 1.83 GHz for one antenna and at 1.77 GHz, possibly even below the lower limit of 1.7 GHz for the other. Thus the ideal frequency in regards to maximizing antenna gain would be at about 1.8 GHz, however other limitations, mainly frequency band allocations apply as well. In this project the applicable bands are the free ISM bands as they are not reserved for other purposes [8]. One such band lies between 2.4 - 2.5 GHz, and the closest applicable band below is situated at 868-870 MHz [27], far below the practical range for this application. Thus the usable frequencies are limited to between 2.4 and 2.5 GHz and in that range 2.48 provides the best performance in terms of minimizing losses due to reflection in the antennas. Fitting the entire expected bandwidth of 64 MHz within the ISM band requires the center frequency to be located slightly lower at 2.468 GHz. To avoid leakage outside of the ISM band due to the rather weak band pass filters of the SDRs it was finally set to 2.45 GHz. This is the main disadvantage of using the Yagi-Uda antennas compared to the patch antennas, looking at Fig. 3.8b a negative peak is apparent around 2.4 GHz for both antennas, meaning that they are far better matched to the impedance at the frequencies the radar system operates at. The lower half of each subfigure in Fig. 3.8 show the S12 and S21 parameters corresponding to the isolation between the antennas. While they appear rather similar around -40 dB, these values, especially in the case of the Yagi-Uda antennas, are not to be entirely trusted as they were taken inside a normal electronics workshop with walls and large metal surfaces within the antennas near field that likely skew the results. Thus no conclusions are to be drawn from the S12 and S21 parameters. Since the S11 and S22 parameters measure reflections in the antenna, they should be reliable. The monopole antennas initially used, typical WiFi antennas, were quickly deemed unsuitable as the omnidirectional nature of them meant that energy was always transmitted straight from the transmitting antenna

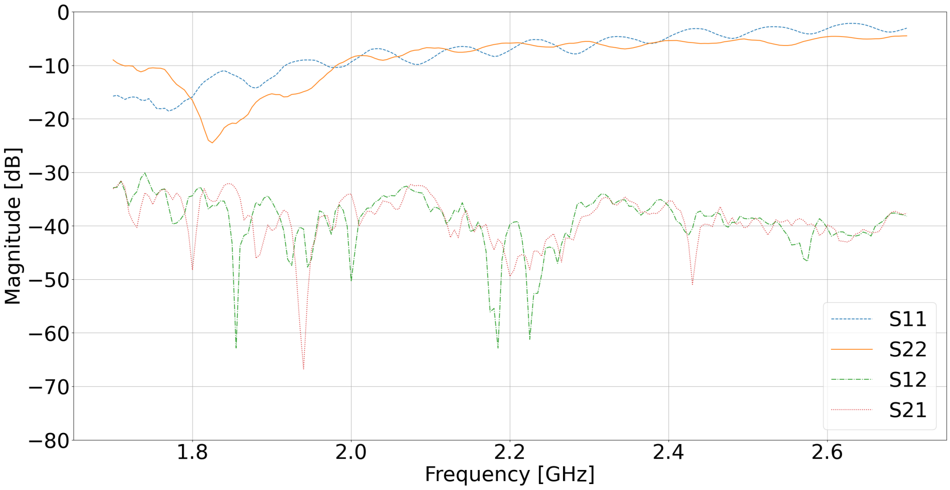

(a) S-parameters for the Yagi-Uda antennas with radome.

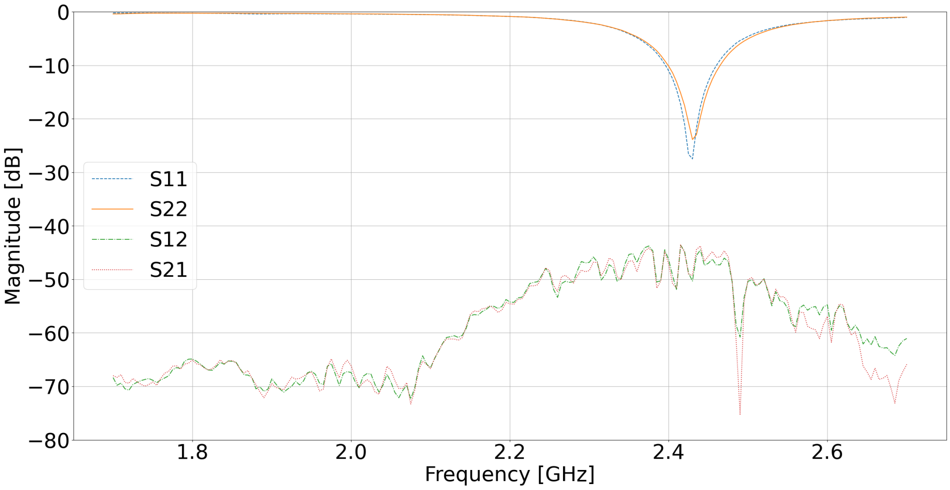

(b) S-parameters for the patch antennas.

Figure 3.8: S-parameters for the Yagi-Uda and patch antennas.

to the receiving antenna causing a short line of sight path, perceived as a massive leakage amplitude in this application. The leakage between the antennas should be much lower for the patch and the Yagi-Uda antennas than for the monopole due to them transmitting a beam directed parallel to the other antenna. Furthermore a narrower beam should attenuate the leakage further since it means less energy is transmitted in the direction of the receiving antenna.

3.5 Signal processing

This section elaborates upon how the signal processing was implemented on the system. Though not all of the methods described in this chapter were implemented into the final range-Doppler processing, due to time constraints, and thus has not been tested on the data presented in the result, it will be included here as it could benefit future implementations by lowering the noise floor. Since the OFDM modulation and demodulation of the sounding signal has already been described in its own section, signal processing will refer to the techniques applied to the signal after demodulation to distinguish the echo signal from the overall received signal. Before delving into these different aspects of the signal processing chain a quick note about the different signals discussed going forward is in order. Firstly calibration measurements, $rx_{cal}(n)$ regards the first stage of the recording when the antennas are pointing upwards towards the sky, providing a proxy for an empty scene. These calibrations were not included into all recordings to save time, as they were not utilized when creating the range-Doppler plots. When $rx(n)$ is mentioned it concerns the normal measurements with the target in the scene. Lastly the background measurements discussed in section 3.5.4 concerns the end sequence of some measurements where the target is removed from the scene, however this is only practically applicable for some measurements using small targets. These different parts are, when applicable, all parts of the same recording to avoid phase errors stemming from the phase difference between the transmitter and receiver being random but constant each time the measurements are started.

3.5.1 Standard method

In this thesis the measurements denoted as standard, calculates the impulse response by extracting a sequence from the received data and dividing it by the transmitted sequence. Due to the simple nature of the signal processing these impulse responses contain both the response from the leakage signal and the echo as well as high noise floors. The range-Doppler plots presented in the results are made by constructing a data frame in fast- and slow-time from these measurements and windowing it with a Hann window in both dimensions. The data frame is then run through a discrete FFT in slow-time to yield the range-Doppler image.

3.5.2 Normalisation

Normalisation aims to remove most of the effect of signal leakage between the transmitting and receiving side of the radar setup. The working principle follows the associative law of the convolution described in section 2.7.3 under the assumption that the effect of signal leakage is constant regardless of whether the antennas are aimed at a target or not. Thus it can be modeled as

$$rx(n) = [tx(n) * h_{channel}(n)] * h_{system}(n), \tag{3.2}$$

$$rx(n) \xrightarrow{\mathscr{F}} RX(f), \tag{3.3}$$

$$RX(f) = TX(f) \cdot H_{channel}(f) \cdot H_{system}(f), \tag{3.4}$$

$$\frac{RX(f)}{TX(f)} = H_{channel}(f) \cdot H_{system}(f). \tag{3.5}$$

In (3.2) through (3.5) $H_{system}(f)$ concerns the transfer function inherent to the radar setup, i.e. that describing the signal leakage. Since the main concern of the radar is to find the target, $H_{system}(f)$ is not of interest and mainly pose a problem since it risks hiding the response from the target as it likely produces a larger signal at the receiver due to the shorter path traveled in comparison to the echo signal. To mitigate this, a measurement without an echo is used for normalisation, henceforth referred to as calibration data. The calibration data has been recorded by aiming the antennas towards the sky since this will produce the same leakage as if it was pointed at a target but will not produce an echo since there is nothing in the signals path that can reflect the signal, at least not using the power levels applicable to this system. Thus it is assumed that the calibration measurements will only be the convolution of the transmitted signal and the radar setup impulse response yielding an FFT as

$$RX_{cal}(f) = TX(f) \cdot H_{system}(f), \tag{3.6}$$

which gives that the normalised transfer function for the system can be obtained by dividing the received signal during calibration with the transmitted signal, in the frequency domain, and as such the transfer function and thus by extension the channel impulse response can be described as

$$H_{system}(f) = \frac{RX_{cal}(f)}{TX(f)}, \tag{3.7}$$

$$H_{channel}(f) = \frac{\frac{RX(f)}{TX(f)}}{\frac{RX_{cal}(f)}{TX(f)}} = \frac{H_{channel}(f) \cdot H_{system}(f)}{H_{system}(f)}, \tag{3.8}$$

$$H_{channel}(f) \xrightarrow{\mathscr{F}^{-}} h_{channel}(n). \tag{3.9}$$

(3.8) provides the basic mathematical background for the normalisation process, and afterwards, ideally the effect of the leakage should be removed and only that of the target echo and the surrounding scene should be left.

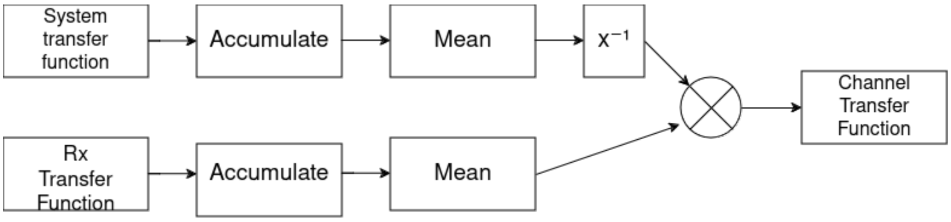

(a) Averaging function MK2.

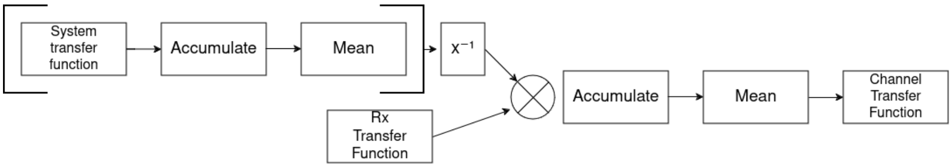

(b) Averaging function MK4.

Figure 3.9: Averaging functions. Accumulate means the consecutive signals are summed up, mean concerns the sum being divided by the number of elements and x^{-1} results in the inverse of the incoming signal.

3.5.3 Averaging

Averaging aims to remove the effects of random noise on the signal and thus lower the noise floor. In practice it has been achieved using two separate but similar methods. The reasoning for using the two has been to evaluate which one performs best when applied to our measurement data, however they do perform rather similarly. The two methods are illustrated in Fig. 3.9.

As can be seen in both Fig. 3.9a and Fig. 3.9b they include normalisation with the system transfer function as well as averaging over several chirps to remove the effect of noise. The main difference however being how the averaging is structured. Fig. 3.9a shows a model where a given number of sequences from the receive signal, each divided by the sounding signal to form transfer functions, are summed up and divided with the averaged transfer function based on the calibration data to create a normalised mean. Fig. 3.9b is instead an approach where the mean of the calibration data transfer functions is calculated beforehand and each individual receive signal transfer function is divided by this average before being summed and averaged to create a normalised mean.

3.5.4 Delta measurements

There is one final piece of signal processing that should be described. The so called delta measurement regards the signal when the previous frame has been subtracted from the target scene. It aims to remove the effect of the stationary environment around a moving target from the resulting data, since these should be constant between two closely located sequences thus leaving only results from moving targets.

It utilizes the distributive properties of the signal composition as described in section 2.7.3. It is assumed that the return signal is composed of the superposition of the echoes from the target as well as the echoes from the surrounding environment. It can be described as

$$rx(n) = tx(n) * h_{moving,target}(n) + tx(n) * h_{stationary,background}(n). \tag{3.10}$$

This is utilized in the creation of the range-Doppler plots called delta. They are calculated in the same way as in the standard procedure but each received sequence $rx(n)$ has had the previous impulse response $rx(n-1)$ subtracted, yielding

$$\begin{gathered} rx(n) - rx(n-1) = (tx(n) * h_{moving,target}(n)+ \\ tx(n) * h_{stationary,background}(n)) - (tx(n-1) * h_{moving,target}(n-1) \\ +tx(n-1) * h_{stationary,background}(n-1)). \end{gathered} \tag{3.11}$$

The transmitted signal $tx(n)$ is constant for all sequences, thus

$$tx(n) = tx(n-1). \tag{3.12}$$

The stationary background should remain constant between two adjacent sequences as well, meaning that

$$h_{stationary,background}(n) \approx h_{stationary,background}(n-1). \tag{3.13}$$

Inserting (3.12) and (3.13) into (3.11) gives

$$\begin{gathered} rx(n) - rx(n-1) = \\ (tx(n) * h_{moving,target}(n) + tx(n) * h_{stationary,background}(n)) - \\ (tx(n) * h_{moving,target}(n-1) + tx(n) * h_{stationary,background}(n)), \\ \\ rx(n) - rx(n-1) = \\ tx(n) * h_{moving,target}(n) - tx(n) * h_{moving,target}(n-1), \\ \\ rx(n) - rx(n-1) = \\ tx(n) * (h_{moving,target}(n) - h_{moving,target}(n-1)). \end{gathered} \tag{3.14}$$

Combined with (2.21) this allows for removal of the transmit signal and thus isolation of the impulse response containing only the movement between the two frames, providing further distinction of the echo response from the clutter.

3.6 Description of the measurements

To evaluate the performance of the designed radar system, measurements were taken in various scenarios. Emphasis is put in creating scenes containing pedestrians, cyclists and cars to evaluate how these commonly occurring objects are perceived by the radar. In order to allow for comparison between the effect of sending a Zadoff-Chu sequence and a random data signal all tests were recorded twice, once while transmitting the Zadoff-Chu sequence repeatedly and once while transmitting a 4QAM modulated random data sequence in the same manner. The evaluation constitutes analysis of the measurements in both the range and the Doppler domain. The measurements can be split into three broad categories based on the location of recording. The first set were recorded on a parking lot with a large shipping container, the second set on a cul-de-sac facing the street and the third were recorded on a long sparsely trafficked street.

In the first set three main scenarios are constructed and measured for evaluation of the system. These measurements are taken in the same location with a static prominent target present at a constant range in every scene. The location of recording along with the static target is shown in Fig. 3.10 where the static target is the closest container. The container was measured to be situated 24.5 m from the radar. Three different tests were conducted, where different moving targets moved towards the radar by passing the shipping container and moving into the bore-sight of the radar in a curved path. The moving targets used in this scene were a car, a bicyclist and a pedestrian. Furthermore, the pedestrian case was recorded both with the pedestrian carrying a boat reflector, with side dimensions 30 cm giving it an RCS of 3.74 m^2, and without carrying the boat reflector.

The second set was aimed mostly at investigating a scene with two moving targets going in opposite directions and was taken at rather short range to study how well the targets would stand out from the signal leakage. The scenario is pictured in Fig. 3.11. In order to test how well the platform could distinguish between different moving targets this scene involved two moving targets travelling along a diagonal path in front of the radar such that they met about halfway along the path, relatively close to the center of the radar bore-sight. The test was repeated with two pedestrians walking, two pedestrians running and two bicyclists travelling along the path. An additional test was also conducted in this scene to test how the platform performed with the patch antennas connected. In this test a car of the same model as used in the previous tests was driving away from the radar.

The third set is pictured in Fig. 3.12 and was meant to test the maximum range at which the platform could successfully detect different targets. The targets tested were a car driving away from the radar, starting next to the platform and driving about 150 meters, and a pedestrian walking away from the radar. The pedestrian test was conducted with two different starting positions where the pedestrian started to walk at about 50 m from the platform or at about 100 m from the platform, though the 100 m case is omitted from the results as the pedestrian was not detected at that range.

Figure 3.10: Field of view from the location of the radar for the measurements of the different scenes. The antennas are to the best of the operators ability directed so that the bore-sight is in the center of the closest container, determined to be at a range of 24.5 m by the use of measuring tape.

Figure 3.11: Field of view from the location of the radar for the measurements of the cul-de-sac scenario. The building in the upper left is located approximately 60 m from the test setup.

Figure 3.12: Field of view from the location of the radar for the measurements of the long range scenario. The car in the applicable measurements was started right in front of the radar and drove down the street. In the pedestrian measurements the person started walking from about the location of the mailbox at the left side of the road.

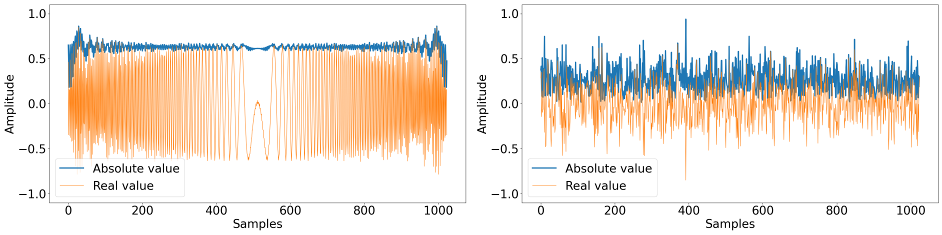

(a) Signal from Zadoff-Chu.

(b) Signal from 4QAM.

Figure 3.13: The transmitted baseband signals generated from the Zadoff-Chu sequence (a) and from the 4QAM sequence (b) and their respective crest factor of 1.37 and 3.10, calculated by (2.4). The shown waveforms are the real part and absolute value of the signals.

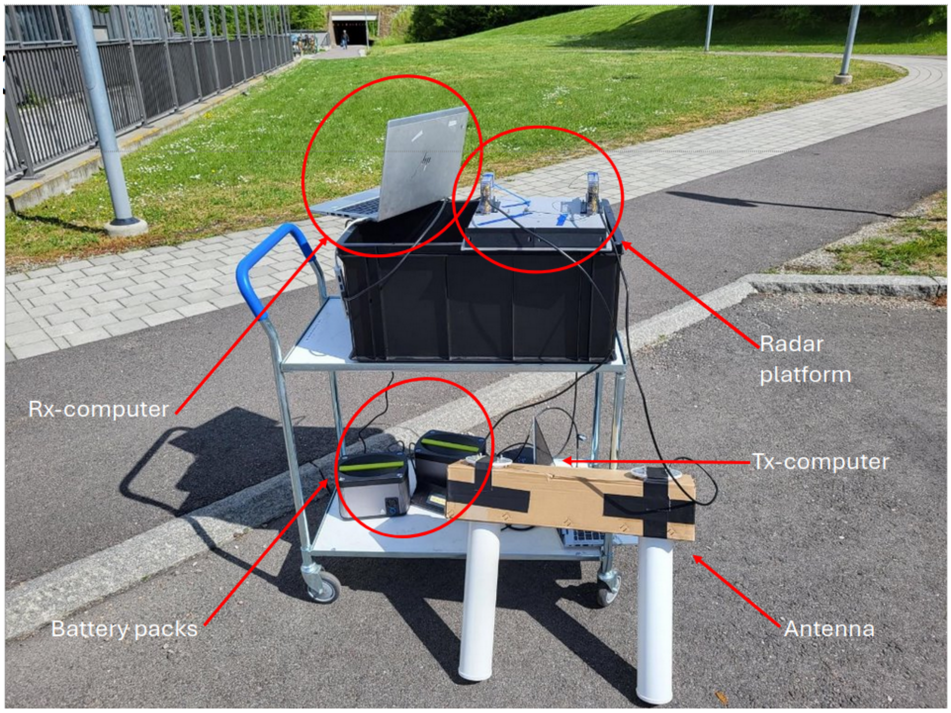

Figure 3.14: The measurement setup.

The two different data sequences, used for the separate recordings of each test, are the Zadoff-Chu sequence discussed in section 3.3.1 and a digitally modulated sequence discussed in section 3.3.2. 4QAM is used as the digitally modulated sequence and it is constructed by generating a random bit sequence once. In this way the same 4QAM sequence is used for all measurements and known beforehand. The resulting transmitted wave forms from the Zadoff-Chu sequence and the 4QAM sequence are shown in Fig. 3.13a and Fig. 3.13b respectively. The system parameters used are listed in Table 3.1.

In order to conduct tests in the field, the test setup pictured in Fig. 3.14 was used. The test setup consists of two computers, for the Tx- and Rx-side respectively, two USB 3.0 to USB type C dongles, or one dongle and one docking station, two lithium-ion battery packs to power the computers and the docking station, a cart and the radar platform. The Yagi-Uda antennas were handheld while the patches were placed in the antenna holder at the front of the radar platform.

System parameters		
Carrier frequency [MHz]	f_c	2450
Sample rate [Msps]	f_s	80
Number of carriers	N	1024
Number of occupied carriers	K	820
Bandwidth [MHz]	BW	80
Occupied bandwidth [MHz]	OBW	64
Sub-carrier spacing [kHz]	Δf	78.125
Automatic gain control	AGC	Active
Number of sequences analyzed	n	10000
Sample bin size [m]	ΔR_{samp}	2.34
Range res. (Hanning window) [m]	ΔR	3
Max unambiguous range [m]	R_{max}	2396
Velocity res. (Hanning window) [m/s]	ΔV	0.62
Max unambiguous velocity [m/s]	V_{max}	±2390

Table 3.1: System parameters.

Chapter 4

Results

The following section will detail the results from a number of measurements recorded by the radar. Most will be visualized as range-Doppler images, as is typical in radar. The range-Doppler pictures in this sections are normalised based on the entire range-Doppler image but are displayed as cropped versions of the image as it includes ranges up to about 2 kilometers and velocities up to about Mach 7, well beyond reasonable tests. The measurements are presented and grouped according to the test conducted and will be followed by a short description of the findings. Before presenting the range-Doppler plots it should be noted that positive velocity is defined here as the radial speed of an object moving towards the radar, while negative velocity is the radial velocity of an object moving away from the radar. Furthermore most of the plots are displayed in groups of four where the top row is the standard range-Doppler plot. The bottom row is referred to as the delta measurement, that is, each sequence in the frame has had the previous sequence subtracted before the range-Doppler plot is constructed, with the purpose of removing any stationary objects and make the moving objects appear more distinctly in the plot. The left column will be from a measurement recorded using the Zadoff-Chu sequence transmitted repeatedly to create the frame, while the right column is the same measurement setup where a predetermined and known 4QAM modulated sequence is transmitted repeatedly instead of the Zadoff-Chu sequence. Note that the Zadoff-Chu and the 4QAM measurements come from separate recordings, as each test was conducted twice, once for each transmit signal, thus small variations might occur between these recordings such as how far into the radar beam a vehicle travelled before steering out of it again. In the same manner the object might also be located at different positions and have different speeds in the two columns. The delta measurement and the standard range-Doppler however are from the same corresponding frame as they only differ in signal processing. Lastly each frame pictured consists of 10 000 consecutive sequences and the amplitudes have been normalised such that the leakage peak at 0 m and 0 m/s is 0 dB.

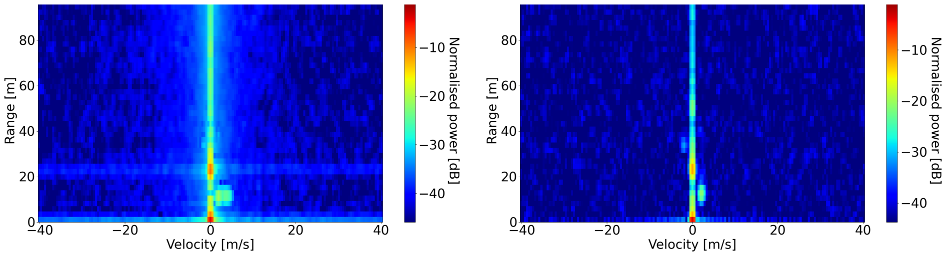

(a) Zadoff-Chu.

(b) QAM.

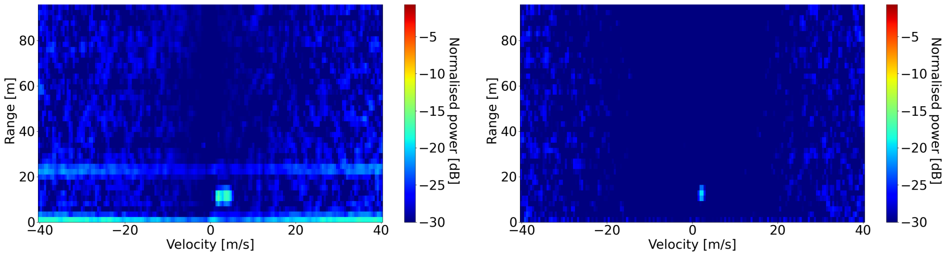

(c) Zadoff-Chu delta.

(d) QAM delta.

Figure 4.1: Range-Doppler of pedestrian holding a reflector walking towards the radar with a steel container in the background.

Target	Zadoff	4QAM
Static [dB]	-9.6	-11.8
Dynamic [dB]	-20.6	-21.2

Table 4.1: Magnitude of targets in Fig. 4.1.

4.1 Pedestrian moving towards the radar

This scene is constructed by having a pedestrian move towards the radar with an initial position to the right of the container in Fig. 3.10 a few meters further back. As soon as the pedestrian passes the container he aligns himself to the bore-sight of the radar, directed towards the center of the container. The recording starts as the pedestrian starts walking and ends when he is few meters from the radar. An overview of the detected magnitudes can be found in Table 4.1 and in Table 4.2 for a person walking towards the radar with and without a reflector respectively. The reflector is a so called boat reflector, consisting of multiple trihedral reflectors with triangular sides and an edge length of about 30 cm giving it an RCS of 3.74 m^2.

Both Fig. 4.1 and Fig. 4.2 show a pedestrian walking towards the radar with and without carrying a corner reflector respectively. Notably the person is clearly visible in all subplots, regardless of the reflector. Though it should be noted that the lower bound on the color grading is slightly different, being set by the median value in the plot assumed to be a good approximation for the noise floor, it gives a

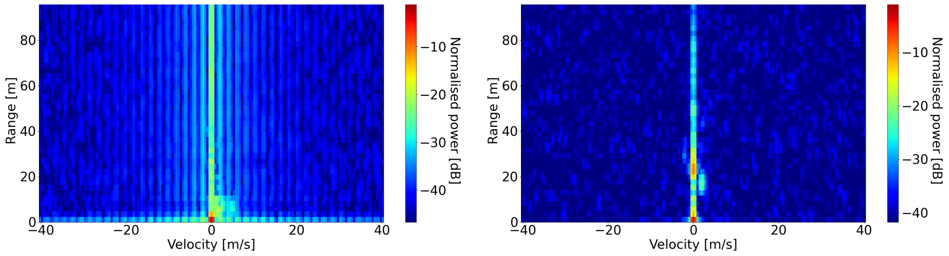

(a) Zadoff-Chu. **(b)** QAM.

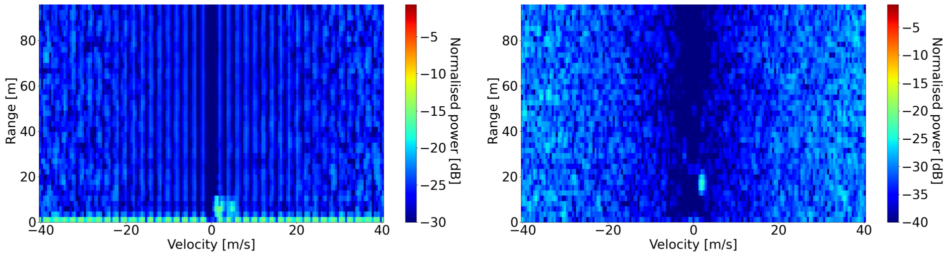

(c) Zadoff-Chu delta. **(d)** QAM delta.

Figure 4.2: Range-Doppler of pedestrian without a reflector walking towards the radar with a steel container in the background.

Target	Zadoff	4QAM
Static [dB]	-20.4	-9
Dynamic [dB]	-19.2	-22.1

Table 4.2: Magnitude of targets in Fig. 4.2.

dynamic range between 45 dB and 30 dB. The magnitude of the target is around -20 dB plus minus 5 dB in all cases with no cohesive distinction between the cases with reflector and those without reflector. In Fig. 4.1a the pedestrian and reflector shows up as a double target of -20.6 dB and -24.5 dB. Furthermore one can see some horizontal spread in magnitude stemming from the container with a strong magnitude of -9.6 dB in Fig. 4.1a, while the subtractions removed the effects of the stationary container Fig. 4.1c still shows this horizontal spread as an artifact. In the delta case the corresponding amplitudes for the pedestrian and reflector is -16.4 dB and -17.9 dB. In the QAM case shown in Fig. 4.1b the container as well as the target appears to have slightly lower magnitudes at approximately -11.8 dB and -21.2 dB respectively and in the delta case -19.5 dB. Other artifacts are found in Fig. 4.2a and Fig. 4.2c, where vertical artifacts are found evenly spaced throughout, slightly obscuring the target in the image. Similar artifacts are found in Fig. 4.8a and Fig. 4.9c suggesting there is some issues with these Zadoff-Chu measurements. The artifacts slightly masks the target and container but they appear to show amplitudes of -20.4 dB and -19.2 dB and -15 dB in the delta case. In the corresponding QAM case the amplitudes are -9 dB for the container and -22.1 dB for the pedestrian as well as -23.2 dB in the delta case. Fig. 4.3 shows a side by side comparison of the same frame as Fig. 4.2a that suffers from vertical artifacts, and the frame used in Fig. 4.1a that does not suffer from these vertical artifacts. To ease the visual analysis in Fig. 4.3 the frame is represented without applying a Hanning window in slow time as is done in the range-Doppler plot. The horizontal axis is the sequence number, from 0 to 10000. Each sequence consists of the impulse response of that received sequence. The depth axis shows the fast time domain, though only showing the first 100 samples since the latter would correspond to a range far beyond the detectable range of the radar. Finally the vertical axis shows the amplitude of the impulse responses. As can be seen in Fig. 4.3a when the frame displays vertical artifacts the amplitude seems to be periodically readjusted, while it stays rather constant in frames that do not display these artifacts as shown in Fig. 4.3b.

4.2 Cyclist moving towards the radar

This scene is constructed by having a cyclist moving towards the radar with an initial position to the right of the container in Fig. 3.10 a couple of meters further back. As soon as the cyclist passes the container he aligns himself to the bore-sight of the radar, directed towards the center of the container. The recording starts as the cyclist is about to pass the container and ends when he is few meters from the radar. The findings detailed below and summarized in Table 4.3.

In this scene a person is cycling towards the radar and Fig. 4.4 clearly shows an object moving towards the radar at about 8 m/s in all cases. Interestingly Fig. 4.4a and Fig. 4.4c also show a target of similar magnitude moving at a similar speed away from the radar at a distance of about 30 m. The actual target to the right has a magnitude of -27.8 dB, the unknown target to the left -30.4 dB and the container

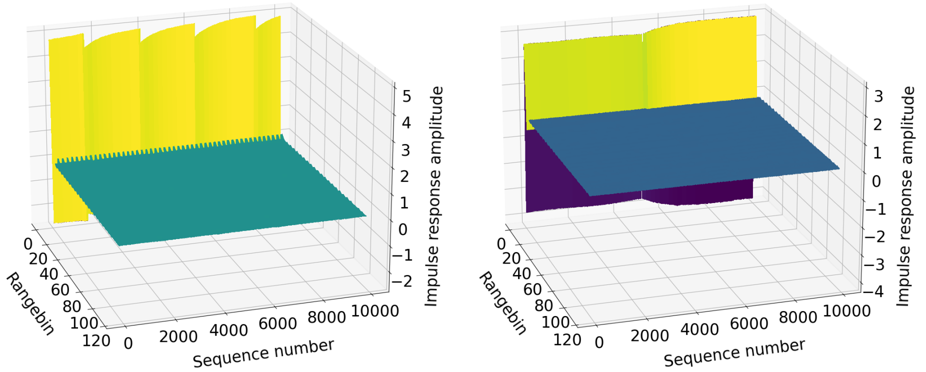

(a) Frame with vertical artifacts. **(b)** Frame without vertical artifacts.

Figure 4.3: 3-dimensional representation of 2 sets of 10 000 impulse responses where one frame suffered from vertical artifacts and the other did not. The x-axis corresponds to the range bins, i.e. the sample delay, the y-axis the amplitude of the impulse response and the z-axis the sequence number.

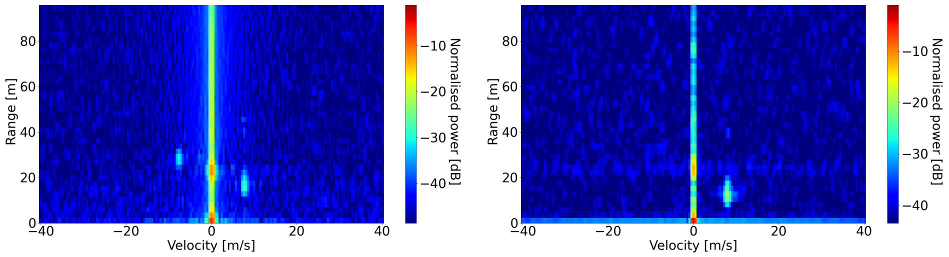

(a) Zadoff-Chu. **(b)** QAM.

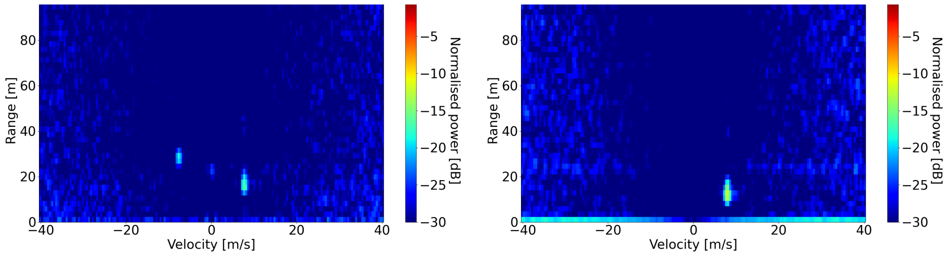

(c) Zadoff-Chu delta. **(d)** QAM delta.

Figure 4.4: Range-Doppler of a cyclist cycling towards the radar with a steel container in the background.

Target	Zadoff	4QAM
Static [dB]	-11.5	-12.0
Dynamic [dB]	-27.8	-20.4

Table 4.3: Magnitude of targets in Fig. 4.4.

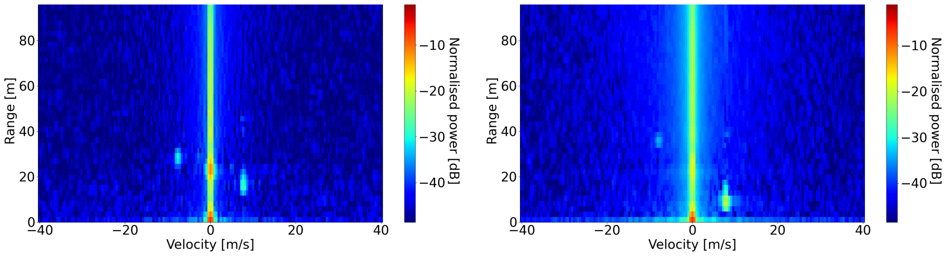

(a) Bicycle t_0 captured with Zadoff-Chu. **(b)** Bicycle t_1 captured with Zadoff-Chu.

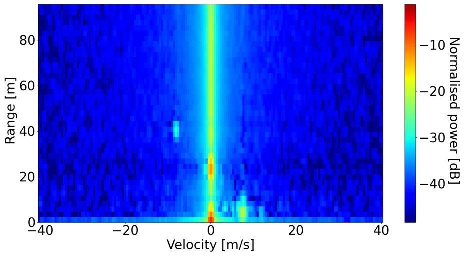

(c) Bicycle t_2 captured with Zadoff-Chu.

Figure 4.5: Time series of range-Doppler delta of a cyclist moving towards the radar. There is 0.65536 s between the the start of each frame.

-11.5 dB. In the delta the cyclist and unknown target have amplitudes of -16.1 dB and -18.8 dB. This unknown target was not part of the test and no note of its presence was taken during the recording of the measurements. However since the stationary object is a shipping container it is likely that it acts as a reflecting plane and that the unknown target is the reflection of the cyclist in that plane. This would explain why it is equidistant and along a straight line from the bicyclist through the stationary target. The unknown target being the cyclist reflection in the container is further supported by the frames in Fig. 4.5. The frames in Fig. 4.5 where taken 0.65536 s apart and shows that the supposed reflection moves in tandem with the cyclist. As the cyclist moves closer to the radar, the unknown target moves further away while maintaining the same but opposite speed, which would be expected from a reflection since the distance between the container and the cyclist increase the closer the cyclist gets to the radar. Fig. 4.4b and Fig. 4.4d show an amplitude of -12.0 dB for the container and -20.4 dB for the bicyclist as well as some horizontal artifacts from the container. The delta measurement in Fig. 4.4d gives an amplitude of -12.0 dB for the bicyclist.

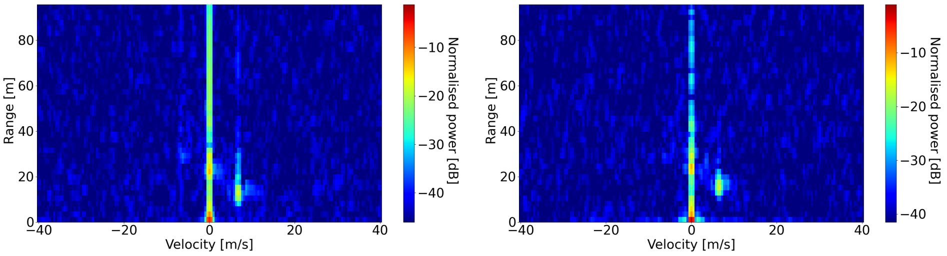

(a) Zadoff-Chu.

(b) QAM.

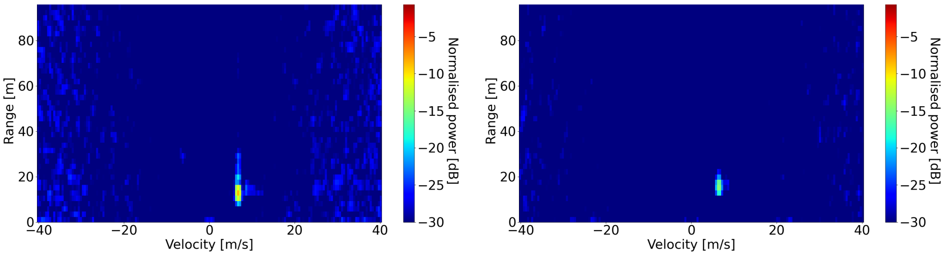

(c) Zadoff-Chu delta.

(d) QAM delta.

Figure 4.6: Range-Doppler of a car driving towards the radar with a steel container in the background.

4.3 Car moving towards the radar

This scene is constructed by having a car moving towards the radar with an initial position to the right of the container in Fig. 3.10 a couple of meters further back. As soon as the driver passes the container he aligns himself to the bore-sight of the radar, directed towards the center of the container. The recording starts as the car is about to pass the container and ends when he is few meters from the radar. A detailed description is found below and the findings are summarized in Table 4.4.

The car moving towards the radar in scene is moving at between 20-21 km/h towards the radar. The container yields an amplitude of -12.9 dB and the car an amplitude of -17.5 dB, in the delta case -8.7 dB from Fig. 4.6a and Fig. 4.6c. The target in Fig. 4.6c the target velocity bin spans between 6.45 m/s to 6.93 m/s corresponding to a speed between 23.2 km/h to 24.9 km/h. Fig. 4.6d displays a wider peak then that observed in Fig. 4.6c, and spans velocities from 5.9 m/s to 6.9 m/s corresponding to 21.5 km/h to 24.9 km/h and has an amplitude of -19.3 dB, while the container has an amplitude of -13.2 dB and the delta measurement yields an amplitude of -17.1 dB.

Fig. 4.7 displays three frames from the measurement where a car drove towards the radar. As expected one can follow the target moving closer to the radar over the course of the measurement. The standard range-Doppler plot was chosen

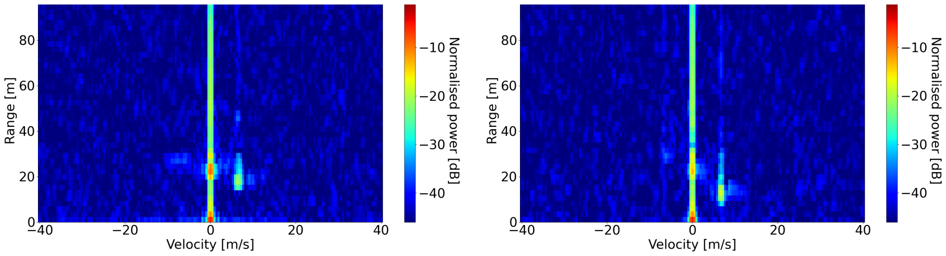

(a) Car t_0 captured with Zadoff-Chu.

(b) Car t_1 captured with Zadoff-Chu.

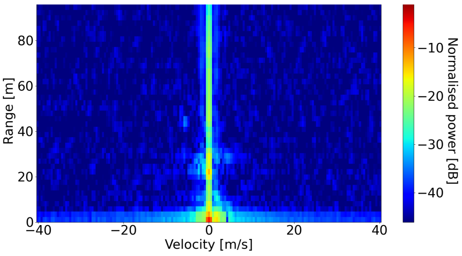

(c) Car t_2 captured with Zadoff-Chu.

Figure 4.7: Time series of range-Doppler delta of a car moving towards the radar. There is 0.65536 s between the the start of the frame at t_0 and the frame at t_1, and 1.96608 s between the frames t_1 and t_2.

Target	Zadoff	4QAM
Static [dB]	-12.9	-13.2
Dynamic [dB]	-17.5	-19.3

Table 4.4: Magnitude of targets in Fig. 4.6.

to display the car's relation to the shipping container and interestingly a weak mirrored reflection of the car can be observed in a straight line through the shipping container suggesting that the car, shipping container and mirror image all were inside the antenna main lobe.

4.4 Cul-de-sac

The following images were captured at a cul-de-sac with the radar facing towards the road to achieve maximal range without any obvious targets. Then each measurement consisted of two persons going towards each other in front of the radar in a diagonal line such that they would have different ranges until they met halfway. This was done using three different modes of travel, namely biking, running and walking, with both the QAM signal and Zadoff-Chu signal tested for each mode,

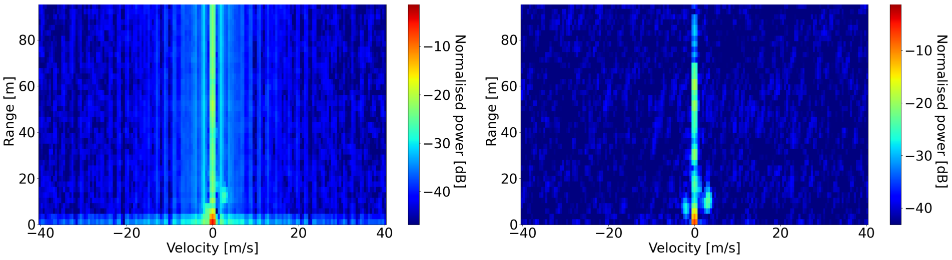

(a) Zadoff-Chu.

(b) QAM.

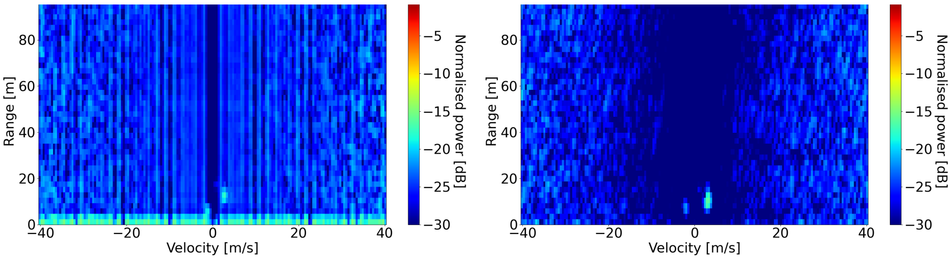

(c) Zadoff-Chu delta.

(d) QAM delta.

Figure 4.8: Range-Doppler of two bicyclists going opposite directions diagonally in front of the radar.

Target	Zadoff	4QAM
Dynamic left [dB]	-27.4	-23.5
Dynamic right [dB]	-24.9	-27.0

Table 4.5: Magnitude of targets in Fig. 4.8.

for a total of six measurements. Each measurement lasted their entire journey from one side to the other but then a frame consisting of 10000 sequences was selected and represented as a range-Doppler image. Thus the timing and the position of the targets may vary between each measurement as the timing was chosen rather arbitrarily, however to ensure some degree of comparability attention was put into finding approximately equal points in the measurements. Each figure contains both the Zadoff-Chu measurement as well as a 4QAM measurement both with and without subtraction of the previous snapshot enabled in post processing, when the previous snapshot is subtracted it is referred to as delta.

Target	Zadoff	4QAM
Dynamic left [dB]	-20.9	-22.8
Dynamic right [dB]	-33.7	-22.5

Table 4.6: Magnitude of targets in Fig. 4.9.

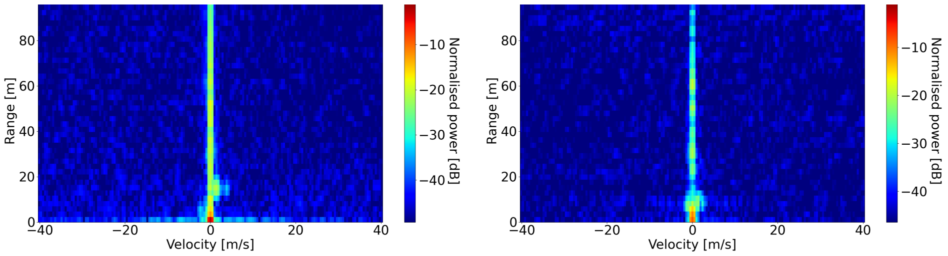

(a) Zadoff-Chu.

(b) QAM.

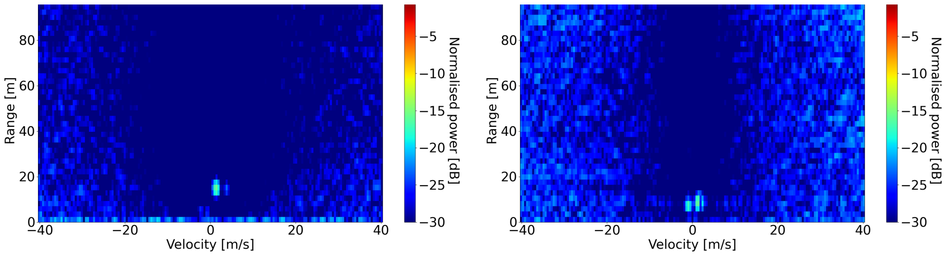

(c) Zadoff-Chu delta.

(d) QAM delta.

Figure 4.9: Range-Doppler of two pedestrians walking in opposite directions diagonally in front of the radar.

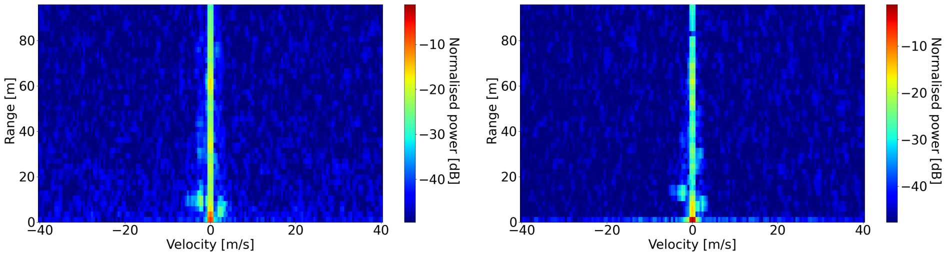

(a) Zadoff-Chu.

(b) QAM.

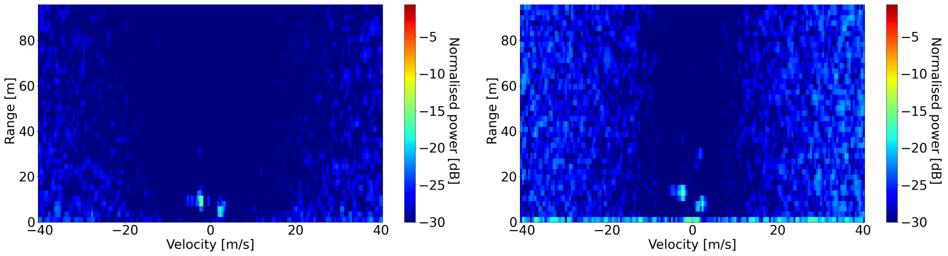

(c) Zadoff-Chu delta.

(d) QAM delta.

Figure 4.10: Range-Doppler of two pedestrians running in opposite directions diagonally in front of the radar.

Target	Zadoff	4QAM
Dynamic left [dB]	-23.5	-26.0
Dynamic right [dB]	-26.2	-27.6

Table 4.7: Magnitude of targets in Fig. 4.10.

Fig. 4.8a shows the two bicyclists moving in opposite directions and a summary of the amplitudes is found in Table 4.5. The bicyclist furthest away yields an amplitude of -27.4 dB while the closest one yield -24.9 dB, though he is difficult to distinguish from the leakage without the delta measure where they yield -17.6 and -18.3 dB respectively. In the QAM recording of the same test the closest and furthest bicyclists yielded -27.0 dB and -23.5 dB and in the delta case they yield -21.8 dB and -16.2 dB respectively.

Fig. 4.9 shows a frame from each recording, Zadoff-Chu and QAM of two persons walking in front of the radar. The amplitude data can be found in Table 4.6 but are detailed in this paragraph. In Fig. 4.9a the pedestrian closest to the radar is barely distinguishable even in the delta case but seems to have an amplitude of -33.7 dB in the standard case and -25 dB in the delta case, while the pedestrian further away yields an amplitude of -20.9 dB in the standard case and -15.6 dB in the delta case. The standard frame from the 4QAM recording shows both pedestrians blend into the noise along the 0 m/s line but the left and right pedestrian yield amplitudes of -22.8 dB and -22.5 dB respectively in the standard case and -17.6 dB and -16.1 dB in the delta case where they are more distinct.

The images in Fig. 4.10 shows two frames from the test when two persons are running. In the Zadoff-Chu recording the runner with negative velocity yield an amplitude of -23.5 dB in the standard case and -16.2 dB in the delta case while the runner with positive velocity yields -26.2 dB and -18.8 dB respectively. For the QAM recording the amplitudes in the standard range-Doppler plot are -26.0 dB for the one with negative velocity and -27.6 for the one with positive velocity, in the delta case they instead yield -15.9 dB and -17.6 dB respectively. The amplitude presented here is summarized in Table 4.7.

In Fig. 4.8 to Fig. 4.10 one can see that both persons are resolvable in all cases, however the pedestrian closest to the radar in Fig. 4.9c gives a rather small power and is harder to distinguish from the noise. Fig. 4.8a as well as Fig. 4.8c also suffers from significantly more noise for unknown reasons. Lastly the noisefloor appears to be between -40 and -50 dB for most of the frames referred to here.

Fig. 4.11 shows a short time series of the two bicycles pictured in Fig. 4.8b and Fig. 4.8d. The time series span a duration of 2.39104 s in total and from Fig. 4.11a one can observe that the bicyclist moving towards the radar is starting the furthest away, as is to be expected. Over the course of the time series the bicyclist cross each other shortly after the frame pictured in Fig. 4.11b and finally they have past each other in the frame pictured in Fig. 4.11c.

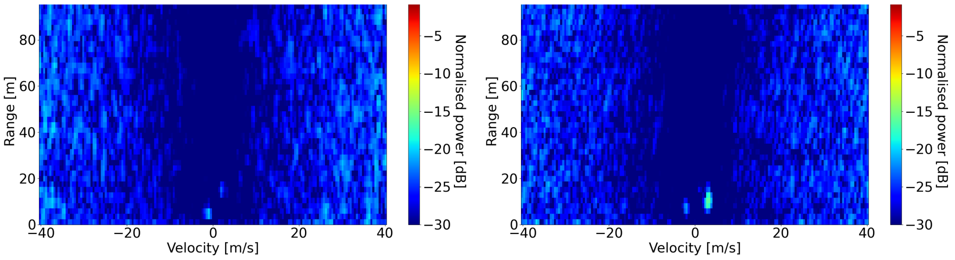

(a) Bicycle t_0 captured with QAM.

(b) Bicycle t_1 captured with QAM.

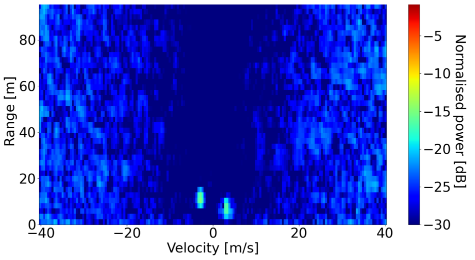

(c) Bicycle t_2 captured with QAM.

Figure 4.11: Time series of range-Doppler delta of bicyclists. There is 1.31072 s between the the start of the frame at t_0 and the frame at t_1, and 1.08032 s between the frames t_1 and t_2.

4.5 Long range measurement

The following measurements were taken on a long straight road with very little traffic and contains two scenarios. In the first scenario a car drives away from the radar and is recorded between approximately 20 and 150 m, though it was not visible in the range-Doppler plot for all of the recording. The second scenario had a pedestrian walking away from the radar, starting at either about 50 or 100 m from the radar. As per usual these scenarios were recorded both with Zadoff-Chu and with 4QAM.

Fig. 4.12a shows the longest range a distinct hit was detected. From the figure it is evident that a car can be detected at 90 m, however the amplitude of the target at -34 dB was only about 6 dB higher than the noise floor at around -40 dB. In the 4QAM recording, pictured in Fig. 4.12b the largest detectable range was about 80 m with an amplitude of -31.6 dB. The difference might be due to circumstance, however the Zadoff-Chu recordings has consistently had slightly higher amplitudes, though as evident in Fig. 4.12a and Fig. 4.12c this also holds for the noise floor.

Due to the smaller RCS of a person when compared to a car the range obtainable when detecting people is smaller as well. Fig. 4.13a show the furthest hit found in the Zadoff-Chu recording of a person starting to walk away from the radar at about 50 meters, and yields distances of 55 m with an amplitude of -32.0 dB,

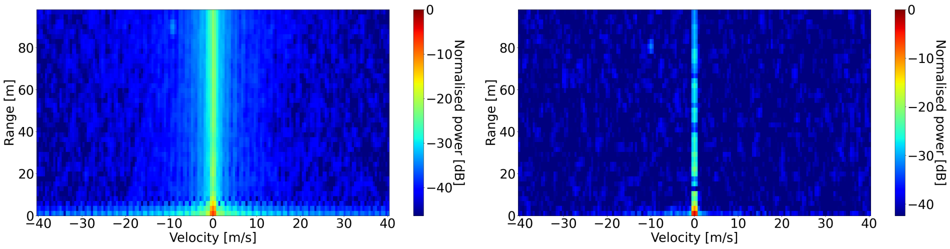

(a) Zadoff-Chu at 90 m.

(b) QAM at 80 m.

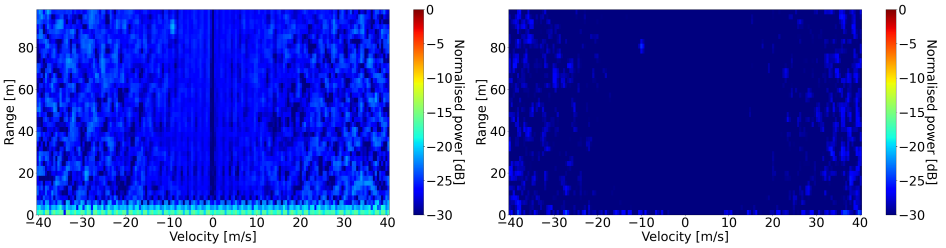

(c) Zadoff-Chu delta at 90 m.

(d) QAM delta at 80 m.

Figure 4.12: Range-Doppler of a car driving away from the radar.

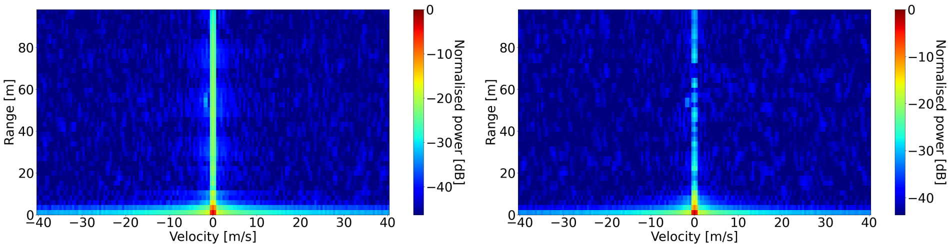

(a) Zadoff-Chu.

(b) QAM.

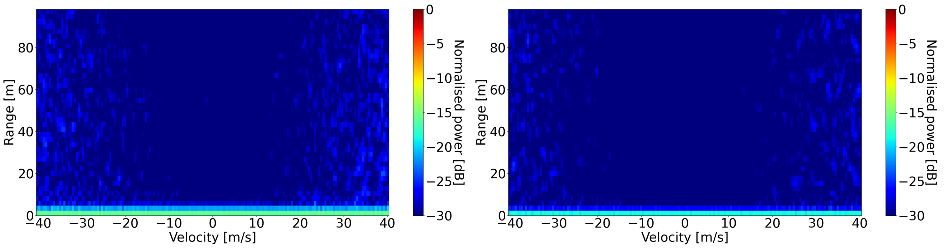

(c) Zadoff-Chu delta.

(d) QAM delta.

Figure 4.13: Range-Doppler of one pedestrians walking roughly 50 m in front of the radar.

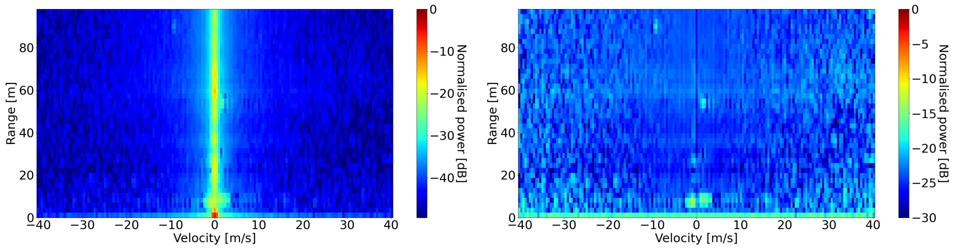

(a) Zadoff-Chu.

(b) Zadoff-Chu delta.

Figure 4.14: Range-Doppler of pedestrians walking roughly 10 m in front of the radar.

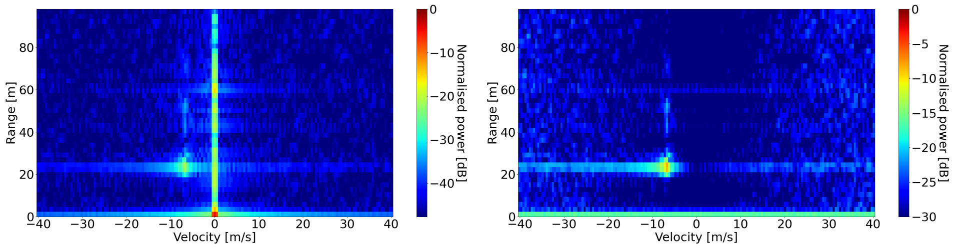

(a) QAM.

(b) QAM delta.

Figure 4.15: Range-Doppler of a car driving away from the radar.

about 8 dB above the noise floor. Fig. 4.13b show a target at 55 m as well, with an amplitude of -32.5 dB, about 9 dB above the noise floor. Interestingly the hits does not show up in the delta measurements.

4.6 Patch antenna measurements

The patch antennas were also tested as a side note to evaluate the feasibility of constructing a system with compact antennas. The measurements were conducted in the cul-de-sac scene described previously. Both the Zadoff-Chu and 4QAM sequences were tested for a moving car in one scene and for two pedestrians walking diagonally in front of the radar in another scene. For the Zadoff-Chu recording, the measurement with the car was error ridden, despite taking two back-to-back measurements, they both suffered from the same vertical artifacts encountered before. Fig. 4.14 and Fig. 4.15 clearly demonstrates that at least for ranges below 30 m, patch antennas are a feasible alternative to Yagi-Uda antennas as both the pedestrians and the car are resolvable in the plots, especially when the delta processing is applied. Additionally the patch antennas provide enough gain to also detect the building at 60 m.

4.7 Signal Processing

Due to time constraints not all methods developed to process the received data ended up in the range-Doppler processing. Fig. 4.16 shows how the impulse response is affected by different signal processing techniques when applied to a measurement with a calibration sequence where the antenna is pointed toward the sky, and then at a building that act as the target. The rightmost column displays the impulse response without normalisation, the leftmost column shows the normalised impulse response without averaging and the middle column, excluding the top row, shows the normalised mean of 1000 sequences in accordance to the methods put forth in section 3.5.3. In the rightmost column the leakage peak has an amplitude of 8.8 dB in all three cases, while the noise floor drops from -13 dB in the top and bottom graphs to -14 dB in the middle row, yielding dynamic ranges of 21.8 dB and 22.8 dB respectively. In the leftmost and middle column the normalisation has caused the leakage peak to have the amplitude 0 dB in all cases. The leftmost column, where no averaging is done gives a noise floor magnitude of -23 dB for the top row and -18 dB for the middle and bottom row. Finally in the middle column where both normalisation and averaging is applied the noise floor drops from -23 dB in the top row to -33 dB for the middle and bottom row. The principal difference between the top row and the lower rows in the leftmost column is that the lower ones are calculated with an averaged calibration response while the calibration response in the top row is based only on one sequence.

4.8 Erroneous measurements

Though the system performs well enough to produce acceptable range-Doppler plots it is not without faults. One such limitation is what will be referred to as "double spikes" in the averaged impulse response. These double spikes are problematic as the secondary peak caused by a phase shift is perceived as a false target in the signal processing of the impulse response. These occur sporadically throughout the measurement and fundamentally limit how many sequences can be included in the frame used to calculate the range-Doppler plot. This limits the length in slow-time and thus the velocity resolution of the final picture. Fig. 4.17 shows a snippet of 9 sequences gathered from a frame of a 1000 sequences where a double spike occurs, in order to show what happens to the receive data during such an occurrence. The lower half of the figure shows the averaged impulse response which displays a secondary leakage peak at around 600 m. As can be seen in the top half of Fig. 4.17 an amplitude spike followed by a phase change happens around 383 sequences into the frame. The frame is taken about 1.66912 s into the same recording used in Fig. 4.7c. It should be noted that each frame used for the range-Doppler images in previous sections of the result were chosen to avoid the presence of double spikes. The amplitude of the primary and secondary leakage peaks are 6.5 dB and 5.4 dB respectively. The amplitude of the primary target is -2.9 dB and the secondary target -5.7 dB, and the noise floor lies about -15 dB.

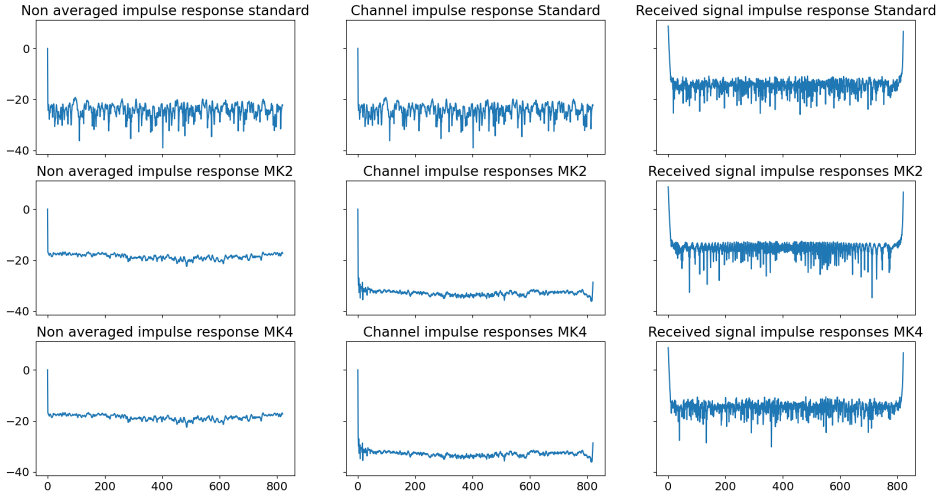

Figure 4.16: Impulse response after different signal processing methods. The x-axis in all plots is sample delay. The top row contains impulse responses without averaging. The middle row uses the averaging denoted MK2 and the bottom row uses the averaging denoted MK4. The leftmost column shows the calibrated impulse responses without averaging, the middle column displays the calibrated impulse response averaged over 1000 sequences while the rightmost column show the impulse responses with neither calibration or averaging. The top right graph show the processing utilized to create the range-Doppler images later on.

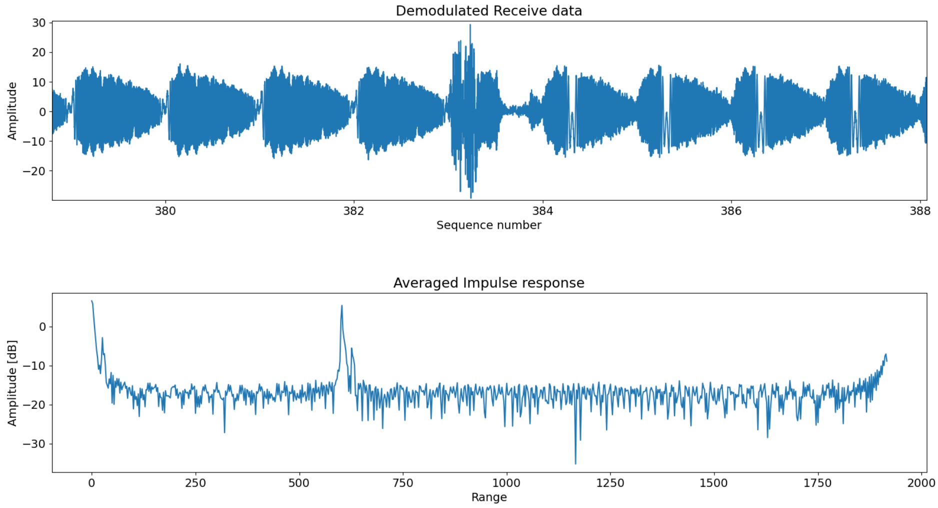

Figure 4.17: The upper graph shows a snippet of sequences 379 to 387 in a frame containing 1000 sequences and the lower graph shows the averaged impulse response of those 1000 sequences. The range is measured in m. The peak around 600 m in the lower figure is the erroneous signal arising from the phase shift in the upper figure. The sequences are from the same recording as Fig. 4.7.

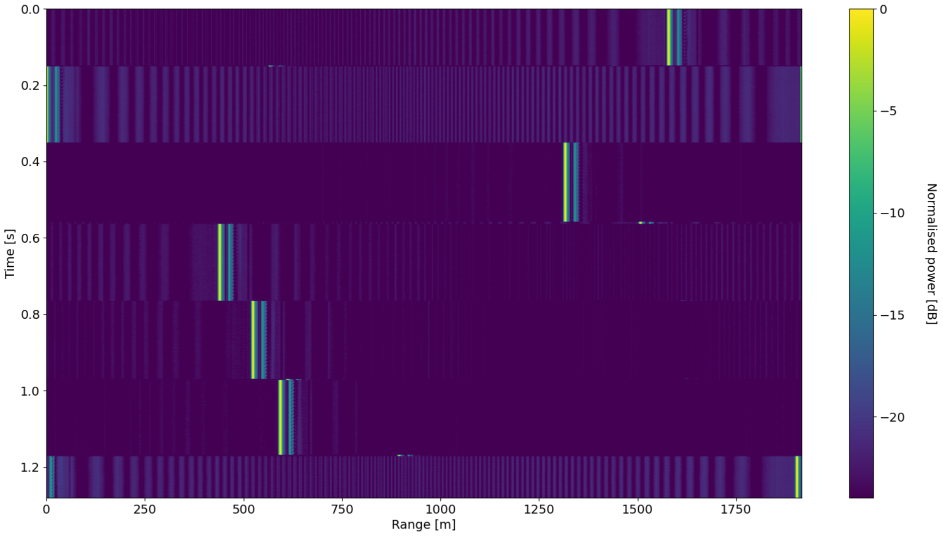

Figure 4.18: Impulse response over time for the recording used in Fig. 4.7 and Fig. 4.17. The colour scale corresponds to the power of the impulse response.

Fig. 4.18 plots the impulse responses for 100 000 sequences and thus shows how the impulse response shifts over time. The impulse responses are given from left to right and the slow-time is given by the y-axis. The entire file is synchronized to the 21st thousand sequence, and as such the the impulse responses that are seen to be consistent between about 0.15 to 0.35 s gives the correct range estimation. As can be seen in the figure the impulse responses appear to be rather consistent with each other over time spans of about 0.2 s after which they shift and remain consistent at another location for about 0.2 s. The plot is normalised to the peak value and the target, a car at about 25 m distance at the time of synchronization, yields an amplitude of the target that is about 13.8 dB, and a dynamic range between the leakage and noise floor of about 25 dB.

Given that the amplitude spike in and subsequent phase shift seen in the top half of Fig. 4.17 occurs at sequence number 28 383 of the corresponding file, and the data in Fig. 4.18 shows 100 000 sequences starting from sequence 1000 of the same file, the amplitude spike from Fig. 4.17 should show up in Fig. 4.18 as a shift of impulse response at

$$\frac{1024 \cdot (28383 - 1000) \text{ samples}}{80 \text{ Msps}} = 0.3505 \text{ s}.$$

Thus one would expect the spike of the impulse responses pictured in Fig. 4.17 to appear as a shift around 0.3505 s in Fig. 4.18. In Fig. 4.18 one such shift is observed shortly before the 0.4 s, supporting the connection between the two observed phenomena.

The top half of Fig. 4.19 displays a snippet of the demodulated signal sequences 473 to 500 from a sample of 1000 sequences from the same recording as Fig. 4.2a and Fig. 4.2c, i.e. one of the figures displaying vertical artifacts. The bottom half instead shows the averaged impulse response from the sample in question. In the lower part of the figure one notices one major difference from Fig. 4.19, that is there is not one but two prominent extra peaks, both of which display the same general attributes as the proper peak at zero range with a target peak shortly to the right. The true leakage peak has an amplitude of 8.4 dB, the higher of the secondary peaks has an amplitude of 1 dB while the smaller secondary leakage peak has an amplitude of -5.9 dB. The noise floor is around -15 dB. The sequences in the sample displayed at the upper half of Fig. 4.19 were chosen such that they span the 0.4 s mark in Fig. 4.20. Another aspect in which Fig. 4.19, differs from Fig. 4.17, is that when viewed over the entire 1000 sequence sample corresponding to the shift between two distinct 0.2 s spans, it displays multiple amplitude spikes while Fig. 4.17 only displays one. This is also the reason as to why the figures display different amount of sequences.

Fig. 4.20 show the impulse responses over time for the same recording as Fig. 4.2a, that is one of the measurements displaying vertical artifacts. Once more the impulse responses appear to remain coherent in 0.2 s intervals, the first one pictured being about 0.4 s though this might be coincidental. An interesting difference can vaguely be found between Fig. 4.20 and Fig. 4.18, namely that the vertical ripples

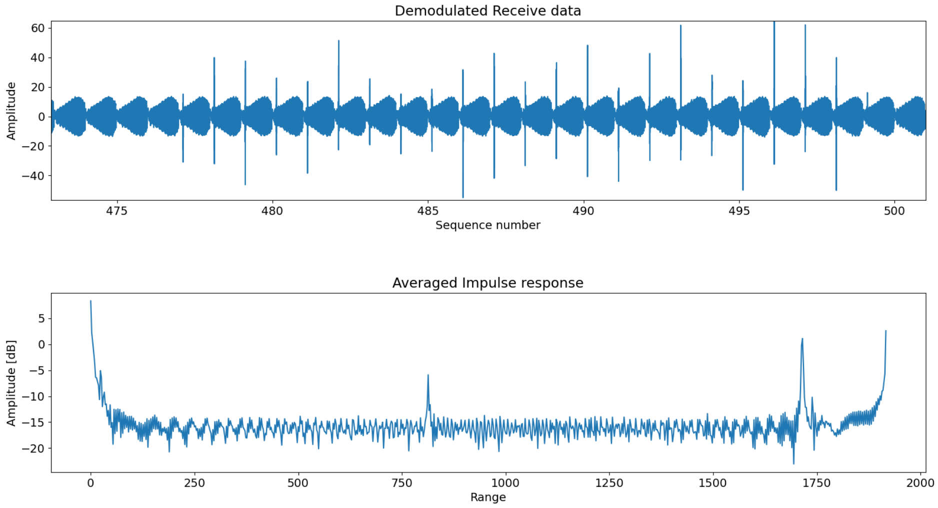

Figure 4.19: The upper graph shows a snippet of sequences 473 to 500 in a frame containing 1000 sequences and the lower graph show the averaged impulse response of those 1000 sequences. The graphs are based on data from the same recording as Fig. 4.2a and Fig. 4.20. The range is measured in m and the peaks at about 800 m and 1700 m are false targets caused by phase shifts similar to that in Fig. 4.17.

that follow the leakage and target spike in both figures have different characteristics. In Fig. 4.18 they are relatively straight horizontal lines of varying width, while in Fig. 4.20 which correspond to a measurement with vertical artifacts, they display more of a zig-zag pattern, corresponding well to the differences seen in Fig. 4.3 where the left picture shows impulses over time for a frame with vertical artifacts in a three dimensional representation and the right image shows a similar sequence from a frame that does not display vertical artifacts, suggesting that the artifacts are related to periodic irregularities in in the amplitude of the impulse responses.

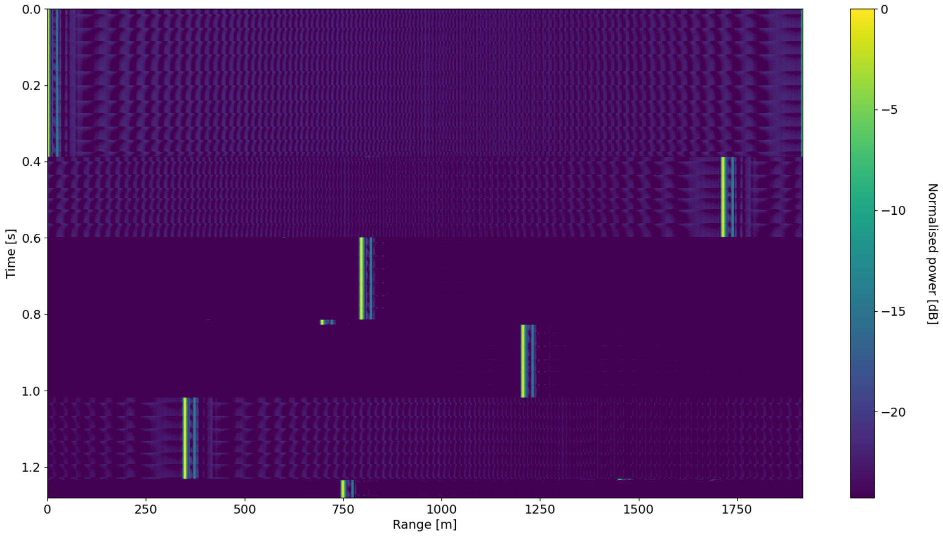

Figure 4.20: Impulse response over time for the recording used in Fig. 4.2a which suffers from vertical artifacts. A notable feature in this graph is the wave like pattern visible in the dark blue vertical lines, suggesting the amplitude is unstable over time. This instability is also visible in Fig. 4.3a that visualise the impulse responses from the same recording.

Chapter 5

Discussion

The system presented in this thesis has many similarities with the different platforms presented in the previous literature but also differs in many ways. The beginning of this section will discuss some of these similarities and differences and how they relate to system performance. After that an analysis and discussion around the limiting factors of the system will follow, and lastly the effect of sending a 4QAM modulated communication like signal instead of the Zadoff-Chu sequence will round up the discussion section.

5.1 Similar platforms

The constructed radar system is in many aspects similar to the 77 GHz software defined OFDM radar presented in [17]. The main differences of the systems aside from parameter choices are the higher operating frequency, the superior hardware and the evaluation methodology used in [17]. The performance of the system in [17] is partly presented as range-Doppler plots of constructed scenes in a semi anechoic chamber for distances under 10 m and velocities between ±4 m/s. For the system constructed in this thesis the measurements are instead taken outside and evaluated for distances under 100 m and velocities between ±40 m/s. The larger range-Doppler domain evaluated in this thesis compared to [17] is mainly due to the inferior performance, largely as a result of the lower bandwidth and sampling speed. However, as the results presented in chapter 4 show, the constructed radar system is capable of detecting and distinguishing between static and moving targets convincingly, much like what is achieved in [17], as long as the reflections of the targets are of sufficient power and the moving target has a high enough radial velocity. For instance, in Fig. 4.6 the leakage, the static container and the moving car are clearly distinguishable for both the Zadoff-Chu signal and the 4QAM signal. To limit the scope of this thesis effort has not been invested in investigating what constitutes sufficient power of reflections for detection. What constitutes a high enough radial velocity is however related to the velocity resolution listed in Table 3.1.

Another similar system is presented in [22]. It is however more similar to a communication system than a radar system since quasi-omnidirectional antennas were used. Apart from the choice of antennas, the system constructed in this thesis closely resemble what was done in [22] since both systems use separate boards for transmission and reception, both systems use the Zadoff-Chu signal in an OFDM scheme and they operate around WiFi frequencies. What is presented in [22] is mainly a proof-of-concept for other researchers seeking to build a channel sounder based on the USRP equipment. Accordingly the evaluation is limited to an investigation of the impulse response for the ultra-wide bandwidth channel. The scope of [22] is quite similar to part of the aim of this thesis, where a similar system is constructed from rather low cost components, however the analysis here is extended to cover the feasibility of using a communication signal for sensing purposes. Furthermore the SDR used in [22], the National Instruments X410 USRP, is much more powerful in regards to the RF characteristics compared to the BladeRF xA9 used in this thesis. Aside from the vast differences in cost of these two, the main difference in regards to radar is the higher bandwidth of 400 MHz and sampling rate of 500 Msps in the X410, meaning far better range resolution can be achieved on that platform as compared with the BladeRF that has a maximum filter bandwidth of 56 MHz and a maximum sampling rate of 122.88 Msps, assuming both platforms were pushed to their respective limit performance wise, and with 821 out of 1024 carriers allocated the minimal range resolution achievable on the BladeRF would, according to (2.12) be

$$\Delta R = \frac{299792458 \text{ m/s}}{2 \cdot \frac{821}{1024} \cdot 56 \cdot 10^6 \text{ Hz}} = 3.33856 \text{ m},$$

while the corresponding for the X410 would be

$$\Delta R = \frac{299792458 \text{ m/s}}{2 \cdot \frac{821}{1024} \cdot 400 \cdot 10^6 \text{ Hz}} = 0.46740 \text{ m}.$$

Given the current implementation, it is the delay that sets the size of the range bins, and as such it is limited by the sampling rate. The same comparison in regards to sampling rate follows (2.14). Applied to the BladeRF it would yield a maximum range resolution of

$$\Delta R_{samp} = \frac{299792458 \text{ m/s}}{2 \cdot \frac{821}{1024} \cdot 122.88 \text{ Msps}} = 1.52148 \text{ m/sample},$$

while the same calculation for the X410 yields

$$\Delta R_{samp} = \frac{299792458 \text{ m/s}}{2 \cdot \frac{821}{1024} \cdot 500 \text{ Msps}} = 0.37392 \text{ m/sample}.$$

Depending on the application though the vast different price range of the SDRs might position the radar platform proposed here as a viable option for low budget applications. Furthermore, the radar platform proposed in this thesis should be rather easy to adapt to another SDR as well as most of the processing takes place off-chip, thus it is rather flexible as it could, to an extent, be scaled in accordance to the application requirement by changing the SDR used to implement it. The downside of this flexibility is however that the data rate between the SDR and the computer can become cumbersome and pose a bottleneck for the system as discussed in section 3.1.3, especially as the currently used SDRs only interface via USB 3.0. This issue arises in a large portion of the literature listed in section 1.3 as well, being noted in both [22] and [23] as a reason for employing real time processing. Very little reliable data was successfully gathered at sampling rates above 80 Msps with the radar platform proposed in this thesis. This suggests that there is good reason to implement real-time processing in such a system in the future in order to get as good a performance as possible from the SDR, though it does make the platform less flexible.

A glimpse into possible usage scenarios for a system like the one constructed in this thesis is given in [13] where several radios, similar to the receive chain in the proposed system, are distributed in a room to effectively create a large multi link channel sounder. The SDRs utilized in the system put forth in [13], the NI-USRP 2953r, has a sampling rate of 200 Msps, which is considerably higher than the BladeRF but they are comparable in other aspects, notably it has a slightly smaller instantaneous bandwidth. Assuming a similar system implementation as the one proposed in this thesis, that should correspond with the USRP achieving significantly smaller range bins due to the higher sampling rate, but a slightly worse range resolution. Another major difference between the platform proposed here and that in [13] is the size of the antenna. The platform in [13] utilizes patch antennas which has a much smaller form factor than the Yagi-Uda antennas, used to achieve enough gain in the platform proposed here. The larger form factor in this proposed platform will limit its feasibility in many scenarios such as a large intelligent surface as it would cause quite an obstruction in the environment it is placed, in a way that patches do not. However the measurements in section 4.6 suggests that patch antennas can be a feasible alternative at short ranges which would allow for a wider range of applications due to the smaller form factor.

Another channel sounder that shows similarities to the proposed system is found in [14] where a distributed system utilizes a Zadoff-Chu signal with OFDM modulation for channel sounding in an industrial environment. In their research they encounter similar problems of loss of calibration after restart as has been described in section 4.8 and that will be elaborated on further in section 5.2. In [14] they state that this require recalibration due to reinitialization of the transmit and receive chains, as the new random phase will have a vastly negative impact on positioning algorithms [14, p. 7]. This is somewhat mitigated in the system put forth in this thesis as it is much simpler, in that it has a practically co-located transmitter and receiver and only one receiver at that, thus negating the need for complex algorithms in favor for simple delay calculation that should be rather simple to correct for in post processing, especially if some sort of flag signal was implemented in the hardware to indicate the timing of the restarts. Furthermore the system in [14] supports various ratios of sub-carrier allocation. The effect of altering the ratio of allocated sub-carriers has not been investigated thoroughly here but rather set to about 80% in accordance to standard practice. However it is suggested by (2.9) that increasing the amount should yield larger OBW which might be beneficial, though it also risks tapering the edges due to filtering effects. The effect of size of sub-carrier domain is also discussed by [7], that concludes that in the case for WiFi sensing the larger sub-carrier domain of 5 GHz WiFi appears to account for most benefits encountered when applied to occupancy counting.

The results prove that it is possible to detect objects that are at least the size of an adult male and likely smaller at moderately short ranges of 55 m or less. By using the radar range equation (2.10) in decibel form, and assuming wavelength, transmit power, antenna gain and radar cross section are constant for a given target one can interpolate the receive power for a given range. Using such an interpolation and knowledge of the systems dynamic range one can calculate an approximate maximum distance at which a given target can be detected since it is only related to the power in relation to the leakage and noise floor. Doing this based on two frames from the recording used in Fig. 4.6a gives

$$\begin{aligned}6.13\text{ dB} = {} & P_t\text{ [dB]} + G_t\text{ [dB]} + G_r\text{ [dB]} + 2\lambda\text{ [dB]} \\ & +\sigma\text{ [dB]} - 33\text{ dB} - 4\cdot 10\log_{10}(16.35),\end{aligned}$$

and

$$\begin{aligned}9.6\text{ dB} = {} & P_t\text{ [dB]} + G_t\text{ [dB]} + G_r\text{ [dB]} + 2\lambda\text{ [dB]} \\ & +\sigma\text{ [dB]} - 33\text{ dB} - 4\cdot 10\log_{10}(11.7).\end{aligned}$$

The leakage level was not entirely constant in the frames observed, it was 0.1 dB higher in the latter case. Assuming this is either an error or due to the transmit power being slightly higher a correction term of -0.1 dB is added at the right side of the latter equation,

$$\begin{aligned}&6.13\text{ dB} + 33\text{ dB} + 4\cdot 10\log_{10}(16.35) = 87.67\text{ dB} \\ &= P_t\text{ [dB]} + G_t\text{ [dB]} + G_r\text{ [dB]} + 2\lambda\text{ [dB]} + \sigma\text{ [dB]},\end{aligned}$$

and

$$\begin{aligned}&9.6\text{ dB} - 0.1\text{ dB} + 33\text{ dB} + 4\cdot 10\log_{10}(11.7) = 85.23\text{ dB} \\ &= P_t\text{ [dB]} + G_t\text{ [dB]} + G_r\text{ [dB]} + 2\lambda\text{ [dB]} + \sigma\text{ [dB]}.\end{aligned}$$

The slight difference between the calculated constants might very well be due to the assumption of constant radar cross section not holding up. This is likely due to the driving pattern of the car which turns into the boresight of the radar beam after passing the container. Due to the car not driving in a straight line, the radar would see it from slightly different angles at different times of the recording which could explain the differences. Given that the dynamic range was found to be about 45 dB and the leakage 21.7 dB, the threshold for detection would be about -23.3 dB. Though looking at the range-Doppler plots in the results it might be hard to distinguish a target at just above -45 dB from the random noise specks at -40 dB.

Thus using -40 dB below the leakage peak as the threshold for detection could be a more sensible choice. Using the lower of the two constant estimates and a lower threshold for detection of -40 dB as a conservative approximation and assuming the car was driving in approximately the same direction as in the frame yields

$$21.7\ \mathrm{dB} - 40\ \mathrm{dB} = -18.3\ \mathrm{dB} = 85.23\ \mathrm{dB} - 4 \cdot 10\log_{10}(d_{max,zdf}).$$

Solving for d_{max} gives

$$d_{max,zdf} = 10^{\frac{103.53}{40}} = 387.48\ \mathrm{m}.$$

The same mathematical reasoning applied to the corresponding 4QAM measurements yields

$$24.6\ \mathrm{dB} - 40\ \mathrm{dB} = 88.35\ \mathrm{dB} - 4 \cdot 10\log_{10}(d_{max,qam}).$$

Solving for d_{max} gives

$$d_{max,qam} = 10^{\frac{103.75}{40}} = 392.4\ \mathrm{m}.$$

Given the uncertainties in the interpolation this suggests that there is no significant difference between transmitting a 4QAM modulated data signal or a Zadoff-Chu sequence in terms of maximum range. This is especially interesting in regards to [6], that finds that theoretically an OFDM system would perform practically the same as a chirp sequence based one given an infinite chirp time. It suggests that the system, regardless of choice between Zadoff-Chu or 4QAM could approach the performance of a similar FMCW radar given long chirp times. This is further supported by [5] that concludes that FMCW systems and OFDM systems could achieve similar performance with the caveat that OFDM based systems are less resilient to interference. However the crest factor calculated in Fig. 3.13 shows significant difference between the two sequences with the random data sequence having almost twice as high a crest factor. A larger crest factor suggests that more backoff is necessary in the amplification stage to avoid clipping or in the worst case destruction of components, thus the crest factor suggests that the Zadoff-Chu sequence can be transmitted with higher gain, thus allowing for longer ranges. Furthermore the numbers should be considered with caution as 300 m do appear to be quite high for such a system, and given the fact that the platform has only been tested on ranges of up to about 90 m there is no data to support such a claim. Furthermore these calculations are based upon the range-Doppler images, and as such include quite some signal processing gain. It is not unlikely that the received signal amplitude might be too low to detect before that. If that should be the case the signal processing gains might not have any effect on detection.

Investigating two frames from the same recording as in Fig. 4.2b, in which a pedestrian is walking towards the radar without a reflector in the same manner as above, gives the constants 85.94 dB and 86.26 dB and receive powers of 4.4 dB and 7.4 dB respectively for frames about 0.6 s apart. Using the smallest constant as before gives an estimated maximum detectable distance of

$$d_{max,qam} = 10^{\frac{102.54}{40}} = 366.0\ \mathrm{m}.$$

Unfortunately a good comparison with the corresponding Zadoff-Chu recording is not feasible due to the vertical artifacts present in Fig. 4.1a.

The results also suggests that the constructed radar system is capable of rather accurate velocity estimation, though it suffers from rather low precision as the velocity bin resolution in a frame of 10 000 sequences is only about 0.5 m/s. However since the system is continuously transmitting sequences, the size of 10 000 is rather arbitrary as it is only applied in post processing of the raw data. As such there is nothing that fundamentally limits this size, though glitches and similar erroneous data usually put an effective limit over how many sequences can be included before the quality of the result deteriorates. An example of this can be seen in Fig. 4.2a where artifacts seems to arise from periodic amplitude fluctuations in the peak amplitude of the impulse response.

The range-Doppler processing utilizes the received impulse response in its most simple form, after synchronization and relevant demodulation, the incoming sequence is simply divided by the transmitted to yield the transfer function and the discrete inverse Fourier transform is performed to yield the impulse response that is placed in the range table.

5.2 Coherence interval

Fig. 4.18 and Fig. 4.20 illustrates how the impulse response changes over time for typical measurements and indicates that a substantial change occurs roughly every 0.2 s. This change is analyzed further by looking at the received data at that time which is shown in Fig. 4.17. It looks like the received data stream is interrupted briefly and when it continues the sequence has been shifted, so that the sequences after the change do not match the sequences before the change. In section 3.1.2 the synchronization of the two BladeRF units was investigated and it was concluded that they are synchronized in frequency but not in time. Furthermore the time offset remains constant during operation and changes only when the transmission is restarted. Moreover a change in time between the two units during operation should manifest as a change in phase, which is not what is observed when analyzing the signals in the oscilloscope. This concept is seen in Fig. 3.3 even though the time span is only 10 ns, the signals were observed for a couple of minutes, which should have induced phase shifts roughly every 0.2 s if a time shift occurred between the two units. This further indicates that the problem likely arises not from a subsequent phase shift between the transmitter and receiver, but rather that the disruption in the transmission cause a change in synchronization between the data stream and the transmitter. This phenomenon effectively puts the maximal coherent interval to 0.2 s, preferably slightly below to have some guard interval in time. Even though the signal should be continuous and the frame length is thus arbitrary this effectively puts an upper bound on the frame length and thus also on the velocity resolution in range-Doppler. Given a span of 0.2 s, a sample rate of 80 Msps and a sequence length of 1024, the maximum number of sequences that can be included in a frame is

$$\frac{80 \cdot 10^6 \cdot 0.2}{1024} = 15625.$$

Inserting these findings into (2.17) gives a maximum achievable velocity resolution of the system of 0.3059 m/s. However due to time restraints and lack of suitable test object to verify such fine resolution this remains a theoretical limit and subject for further inquiry.

Investigating Fig. 4.18 and Fig. 4.20 highlights another interesting area for further studies, the impulse response appear rather stable in each 0.2 s span. Given that the leakage peak is unlikely to move and should logically always be at 0 range since it is effectively instantaneous at the sampling rates in question, and given that one knows where each interval starts and ends one could shift the erroneous sequences such that the leakage peak is always at zero range. This would not remove all of the problems with shifting phases, as small specks of leakage and target peaks can be found outside of these 0.2 s spans, for example at around 0.57 s in Fig. 4.20 at the right side of the figure. Despite not correcting for all errors such a signal processing could potentially allow for far longer coherent intervals and thus improve the velocity resolution even more.

5.3 Performance limitations

In general there can be many limiting parameters when trying to achieve the best possible performance in a radar system. It is however not trivial what constitutes good performance, as it is largely dependent on the specific application. Looking at some of the key performance parameters discussed in section 2.6 you could for instance optimize (2.17) for a fine velocity resolution ΔV by increasing the pulse repetition time. Increasing the PRT would however decrease the maximum unambiguous velocity V_{max} according to (2.18). This type of tradeoff where changing one parameter to improve one performance aspect and consequently deteriorate another performance aspect is evident for many parameters.

By looking at the system parameters listed in Table 3.1 a natural approach for improving the performance of the system is by improving both the range resolution of 3 m and the sample bin size of 2.34 m. For the application both the maximum unambiguous range and the maximum unambiguous velocity are sufficient with a large margin. From Fig. 2.4 it is evident that the received power would be way to low for a detection when increasing the range and approaching the maximum unambiguous range. In everyday situations the highest velocity encountered could for example be vehicles on the highway traveling at a speed of about 110 km/h which corresponds to roughly 31 m/s, which is way below the maximum unambiguous velocity. Accordingly the performance of the system is mainly limited by the range resolution and the sample bin size. From a broader perspective, not necessarily limited to the current hardware, the system could be improved in many ways. Effort could for instance be invested in improving the signal-to-noise ratio (SNR) to achieve better performance.

For the system constructed in this thesis one major limiting factor is the speed of the data bus between the BladeRF and the host computer discussed in section 3.1.3. This limitation is mentioned in [23] and the proposed solution to reduce the data rate is to implement real-time processing on the SDR. The sampling frequency is a key parameter as it affects multiple performance aspects and it is directly related to the data rate. Having the ability to increase the sampling frequency would for instance enable a higher bandwidth resulting in a finer range resolution according to (2.12). Furthermore a higher sampling frequency would result in a shorter propagation distance of the EM wave between each sample according to (2.15) and therefore reduce the sample bin size.

5.4 Evaluation of the Zadoff-Chu and the 4QAM signal

Using the Zadoff-Chu signal as the sounding signal should in theory be superior to using a digitally modulated signal such as 4QAM for radar application. This is largely due to the inherently low PAPR of the Zadoff-Chu sequence, as one of the main challenges in OFDM is dealing with high PAPR [9]. In Fig. 3.13 the transmit signal generated from the Zadoff-Chu sequence and the signal generated from a 4QAM sequence are shown and their crest factor of 1.37 and 3.10 respectively, showing that the Zadoff-Chu sequence is superior from a PAPR standpoint. However by using the Zadoff-Chu signal the system is limited to perform only sensing as opposed to joint communication an sensing, which is possible with a digitally modulated sequence, provided that it is known. Therefore it is of great interest to evaluate the radar performance using a digitally modulated sequence in addition to the theoretically favorable Zadoff-Chu sequence. The methodology used in this thesis is not tailored specifically for evaluating potential differences in performance of the two sequences, as the main focus is to evaluate the general radar performance, primarily by analysis of the range-Doppler representations of the results. The normalised power relative to the leakage is stated for the targets in the presented measurements in chapter 4, which could be used as a quantity for comparing how the sequences perform relative to each other. However the data presented for the Zadoff-Chu sequence and the 4QAM sequence are captured in separate measurements and consequently there are variations in the scene to consider when comparing them. In addition to the variations in the scene, there are also variations in the system, where one of the more apparent variations is the usage of automatic gain control.

Chapter 6

Conclusions and further work

In this chapter the conclusions of the project are presented as well as ideas for further work, largely based on what is discussed in chapter 5. The conclusions are presented first followed by further work.

6.1 Conclusions

In this thesis project a 2.45 GHz SISO software defined OFDM radar based on open-source software and affordable off-the-shelf components has been designed, implemented and verified. The design utilized two BladeRF 2.0 micro xA9 SDR units and two Yagi-Uda antennas. Furthermore it was complemented by a signal processing script made in Python and interfaced with the radar platform using GNU Radio. The system proved capable in sensing applications using both a chirp-like Zadoff-Chu sequence and a communication enabling 4QAM sequence as the sounding signal. In particular the utilization of 4QAM provides valuable insights for future endeavors within joint communication and sensing based on affordable off-the-shelf hardware and open-source software. The performance of the system was demonstrated by outside measurements of scenes containing moving pedestrians, cyclists and cars, complemented by a profound static target in some scenes and an additional moving target in the others. The results were quantified and presented mainly by range-Doppler images of the scenes.

The system was tested at ranges of up to about 90 m and proved capable of resolving a pedestrian at about 50 m, and a car at 90 m. the results also conclude that swapping the Yagi-Uda antennas to patch antennas yield satisfactory results at short ranges. Most tests were carried out on shorter ranges of about 25 m and in addition to the previous statement, resolved a bicycle and a stationary shipping container. The pedestrian, cyclist and car are only evaluated when they are in motion, for them to have non-zero Doppler. The signal power of these targets are of roughly the same magnitude as the zero Doppler, which indicates that stationary people, bicycles and cars could be challenging to resolve. The performance of 4QAM and Zadoff-Chu are according to the range-Doppler evaluation very similar with small inconsistent variations in magnitude of the targets between the measurements. Hence the radar performance of the system is not conclusively affected by the use of 4QAM as opposed to Zadoff-Chu. The main bottleneck of the system is rather the insufficient transfer speed between the SDR and the host computer, restricting the sampling speed and effectively limiting the number of usable channels to one per unit. The results has empirically proven that in the case of short ranges of about 50 m, it is feasible to use low cost readily available SDR units as a basis for a system capable of joint communication and radar, with respect to detecting large stationary or moving objects. It is possible that implementation of the signal processing algorithms discussed in section 4.7 could increase the range of the radar platform as it could likely lower the noise floor. However it has also concluded that improvements in the data transfer between the SDRs and the computers is likely required to take full advantage of the SDRs performance capabilities, in essence calling for real time processing or more dedicated hardware.

Furthermore a coherency issue was observed, manifested by a periodic disruption in the transmission, effectively limiting the maximum coherent interval, which otherwise should be arbitrary. The transmitter and receiver are synchronized in frequency with a constant phase shift, indicating that the issue likely is inherent to the configuration of the BladeRF units, which possibly could be addressed in a custom implementation of the onboard FPGA. The effect of the coherency issue on the implemented system is mainly a limitation of the velocity resolution as well as more cumbersome processing of the received data.

6.2 Further work

As demonstrated in Fig. 4.18 and Fig. 4.20 and discussed in section 5.2 the received data appears to change phase about every 0.2 s, likely due to a change in synchronization caused by a disruption in the transmission. As this is a limiting factor some further work on correcting this issue could improve the performance of the radar system, especially in the Doppler domain. Finding the cause of these frequency shifts, likely stemming from the SDRs would also make for interesting further studies.

One key factor limiting the performance of the constructed system is the lack of real-time processing, resulting high amounts of data being passed between the host computer and the BladeRF, to the point where the communication bus is saturated and the full capabilities of the BladeRF are not utilized. For instance 80 Msps is used even though sampling speeds of up to 122.88 Msps are possible. Furthermore the communication bus struggles to satisfy the demands of one channel and the BladeRF supports four channels. Limiting the data transfer could therefore enable multi-channel operation. Future work within the area could for example constitute a custom implementation of the FPGA to enable on-chip real-time processing and consequently reduce the data transfer substantially between the BladeRF and host. Possibly two Rx- and Tx-channels could be implemented opening up for a 2x2 MIMO system enabling further processing of the data.

Bibliography

[1] Karim Abbas. *From Algorithms to Hardware Architectures. Using Digital Radios as a Design Example*. Springer International Publishing, 2023. ISBN: 9783031086922.

[2] *About GNU Radio*. 2024. URL: `https://www.gnuradio.org/about/` (visited on 04/24/2024).

[3] *An introduction to OFDM - Lecture notes in the course Digital communications, advanced course (ETTN01)*. URL: `https://www.eit.lth.se/fileadmin/eit/courses/ettn01/HT2-2017_Rusek/OFDM_lecture_notes_161115.pdf` (visited on 05/15/2024).

[4] Gary Breed et al. "The fundamentals of patch antenna design and performance". In: *High frequency electronics* 3.12 (2009).

[5] Gisela K. Carvajal et al. "Comparison of Automotive FMCW and OFDM Radar Under Interference". In: *2020 IEEE Radar Conference (RadarConf20)*. 2020. DOI: `10.1109/RadarConf2043947.2020.9266449`.

[6] Johannes Fink and Friedrich K. Jondral. "Comparison of OFDM radar and chirp sequence radar". In: *2015 16th International Radar Symposium (IRS)*. 2015. DOI: `10.1109/IRS.2015.7226369`.

[7] Haobin Guan et al. "Experimental Accuracy Comparison for 2.4GHz and 5GHz WiFi Sensing Systems". In: *ICC 2023 - IEEE International Conference on Communications*. 2023. DOI: `10.1109/ICC45041.2023.10278557`.

[8] Mark Harris. *ISM Bands Around the World*. 2023. URL: `https://resources.altium.com/p/ism-bands-around-world` (visited on 04/09/2024).

[9] Neenu Joseph and P. Nirmal Kumar. “Peak Power and Crest Factor Reduction in OFDM Transceiver Using Filtering Method for SDR Application.” In: *National Academy Science Letters* Preprints (2015). DOI: `10.1007/s40009-015-0378-0`.

[10] John D. Karus and Ronald J. Marhefka. *Antennas for all applications.* McGraw-Hill Higher Education, 2002.

[11] Per-Simon Kildal. *Foundations of antenna engineering: A unified approach for line-of-sight and multipath.* Kildal Antenn AB, 2015.

[12] *LMR®-195 Flexible Low Loss Communications Coax.* Times Microwave systems. URL: `https://timesmicrowave.com/wp-content/uploads/2022/06/lmr-195-datasheet.pdf` (visited on 05/21/2024).

[13] Christian Nelson et al. “Large Intelligent Surface Measurements for Joint Communication and Sensing.” In: *European Conference on Networks and Communications (EuCNC) and 6G Summit,Gothenburg, Sweden,– 2023 Joint European Conference on Networks and Communications & 6G Summit (EuCNC/6G Summit)* (2023). arXiv: `2304.12457 [eess.SP]`.

[14] Nelson, Christian and Li, Xuhong and Fedorov, Aleksei and Deutschman, Benjamin J. B. and Tufvesson, Fredrik. “Distributed MIMO Measurements for Integrated Communication and Sensing in an Industrial Environment”. In: Sensors 24.5 (Feb. 2024). DOI: `{10.3390/s24051385}`.

[15] Nuand. *BladeRF 2.0 micro.* URL: `https://www.nuand.com/bladerf-2-0-micro/` (visited on 03/05/2024).

[16] *Nuand GitHub.* 2024. URL: `https://github.com/Nuand` (visited on 04/24/2024).

[17] Clemens Pfeffer et al. “A 77-GHz software defined OFDM radar”. In: *2014 15th International Radar Symposium (IRS).* 2014. DOI: `10.1109/IRS.2014.6869235`.

[18] John G. Proakis and Dimitris K. Manolakis. *Digital Signal Processing.* 4th ed. Pearson Education Limited, 2014. ISBN: 9781292025735.

[19] *radartutorial.eu.* URL: `https://www.radartutorial.eu/02.basics/MIMO-radar.en.html` (visited on 05/07/2024).

[20] M. A. Richards, Jim Scheer, and William A. Holm. *Principles of modern radar.* Radar, Sonar, Navigation and Avionics. SciTech Pub., 2010. ISBN: 9781891121524.

[21] Mark A. Richards and William Melvin. *Principles of modern radar.* Radar, Sonar and Navigation Ser. Institution of Engineering & Technology, 2022. ISBN: 9781839533815.

[22] Michiel Sandra, Christian Nelson, and Anders J Johansson. “Ultrawideband USRP-Based Channel Sounding Utilizing the RFNoC Framework”. In: *2022 IEEE Conference on Antenna Measurements and Applications (CAMA).* 2022. DOI: `10.1109/CAMA56352.2022.10002476`.

[23] Michiel Sandra et al. *A Wideband Distributed Massive MIMO Channel Sounder for Communication and Sensing.* 2024. arXiv: `2403.11856 [eess.SP]`.

[24] Ashish Kumar Sarangi and Amlan Datta. “Capacity Comparison of SISO, SIMO, MISO & MIMO Systems”. In: *2018 Second International Conference on Computing Methodologies and Communication (ICCMC).* 2018. DOI: `10.1109/ICCMC.2018.8488147`.

[25] Mischa Schwartz. “Modulation techniques”. In: *Mobile Wireless Communications.* Cambridge University Press, 2004.

[26] Yoke Leen Sit. *MIMO OFDM Radar-Communication System with Mutual Interference Cancellation.* Karlsruhe: KIT Scientific Publishing, 2017. ISBN: 978-3-7315-0599-0. DOI: `10.5445/KSP/1000061697`.

[27] Karolina Sjöblom Dan & Asp. *Post- och telestyrelsens allmänna råd (PTSFS 2019:1) om den svenska frekvensplanen.* 2019. URL: `https://www.pts.se/globalassets/startpage/dokument/legala-dokument/foreskrifter/radio/pts_allmanna-rad-om-den-svenska-frekvensplanen-ptsfs2019-1.pdf` (visited on 04/09/2024).

[28] Wally H. W. Tuttlebee. *Software defined radio. enabling technologies.* Wiley, 2002. ISBN: 9780470843185.

[29] Masahiro Umehira, Katsuyuki Fujii, and Yasuyuki Okumura. “Radar-Communication Integration System based on PMCW Radar using Zadoff-Chu Sequence”. In: *2023 28th Asia Pacific Conference on Communications (APCC).* 2023. DOI: `10.1109/APCC60132.2023.10460647`.

[30] *What are the Maximum Power Output and Data Transfer Rates for the USB Standards?* URL: `https://resources.pcb.cadence.com/blog/2020-what-are-the-maximum-power-output-and-data-transfer-rates-for-the-usb-standards` (visited on 05/23/2024).

[31] *What are the Maximum Power Output and Data Transfer Rates for the USB Standards?* URL: `https://www.cuidevices.com/blog/usb-type-c-and-3-2-clarified` (visited on 05/23/2024).

[32] *Yagi Tube LTE.* Proscan. URL: `https://www.kjell.com/globalassets/mediaassets/842731_30151_datasheet_en.pdf?ref=15070349CD` (visited on 05/21/2024).

[33] Paul H. Young. *Electronic communication techniques.* Prentice Hall, 2004. ISBN: 0130482854.